Master in Quantum Science and Technology

Digital-Analog Quantum Simulation of Spin Systems in Trapped Ions

Master Thesis

by

Iñigo Arrazola

Director:

Prof. Enrique Solano

Departamento de Química Física
Facultad de Ciencia y Tecnología
Universidad del País Vasco UPV/EHU

Leioa, September 4, 2015

Digital-Analog Quantum Simulation
of Spin Systems in Trapped Ions

Iñigo Arrazola

September 4, 2015

Abstract

We propose a method to simulate spin models in trapped ions, using digital-analog techniques. With a suitable multiqubit gate decomposition in terms of analog blocks and digital steps, we show that the dynamics of the spin-1/2 Heisenberg chain can be implemented in a linear ion array. This digital-analog proposal involves substantially less number of gates than a fully digital approach, making it a good candidate for experimental implementations. Our work may be adapted to different quantum platforms.

Laburpena

Teknika digital-analogikoak erabiliz, ioi harrapatuetan spin sistemak simulatzeko metodo bat aurkezten dugu. Bloke analogikoak eta pauso digitalak tartekatuz, spin-1/2eko Heisenberg ereduaren dinamika ioi kate baten bidez simula daitekela azaltzen dugu. Prozedura digital-analogikoek guztiz digitala den protokolo batek baino ate gutxiago behar ditu, esperimentalki gauzatzea erraztuz. Gure lana beste plataforma kuantiko batzuetara moldagarria izan daiteke.

Resumen

Proponemos un método para simular modelos de espines en iones atrapados, mediante técnicas digital-analógicas. Usando una descomposición en puertas multiqubit, demostramos que es posible implementar la dinámica del modelo de Heisenberg de espín-1/2 en una cadena de iones. La propuesta digital-analógica requiere un menor número de puertas que un protocolo completamente digital, facilitando su realización experimental y su adaptación a diversas plataformas cuánticas.

Contents

Introduction

Physics consists in the effort to reduce and translate natural phenomena to the language of mathematics through the observation of empirical evidence. To achieve that, we build mathematical models, with which we are able to predict, describe and understand nature. And then, in order to corroborate these models, we confront their predictions with experiments. However, extracting meaningful predictions from the mathematical model will often require to perform calculations that, while technically simple, take a lot of time. Therefore, we build machines, computers, that are able to do these calculations faster than any human being, using algorithms that are written in a binary language. Since the 1970's, digital computers, that process and store information using bits, have shrunk by a factor of 2 every 2 years. Thanks to them, over the past 40 years, we have been able to compute more difficult problems, faster and with tinier machines. Nevertheless, this computer hardware improvement will eventually reach the limits of miniaturization at atomic levels, where quantum effects become significant. The theory of quantum computation aims at taking advantage of the eventual entering into the quantum regime, by using quantum mechanical phenomena to carry out computations in a different and presumably more efficient way.

Quantum mechanics is the theory that describes processes that involve atoms or electrons, with applications that go from the LEDs to medical imaging such as magnetic resonance imaging (MRI), including microprocessors, building blocks of modern computers. In some branches of quantum mechanics, such as condensed matter or quantum chemistry, problems that involve many-body quantum systems rapidly reach the computational limit and become intractable. This is due to the exponential growth of the quantum degrees of freedom with the number of particles. We are left with a cumbersome problem: we have models that describe the physics of a few particles, but we do not know whether their predictions are correct when more particles are involved. Then, how could one check the validity of these models?

In this context, R. Feynman proposed the idea of employing fully-controllable quantum systems to simulate and compute other quantum systems, i.e., to use these exponential degrees of freedom as a resource for computation [1]. Several scientific fields such as the already commented quantum computation and quantum simulations are based on this idea. Pioneering works by P. Shor [2], establishing the first quantum algorithm to efficiently factorize numbers, C. H. Bennett and G. Brassard [3, 4], proposing the first quantum teleportation protocol and the field of quantum cryptography, and the

proposals of J. I. Cirac and P. Zoller [5], for the engineering of the first controlled-NOT quantum gate in a quantum platform, have contributed to make the field of quantum computation mature and promising.

Although in the last two decades quantum technologies have grown rapidly, the number of fully-controllable quantum systems that we are yet able to manage is too small for the construction of a universal quantum computer. However, the efforts placed in quantum technologies have already provided us with sufficient tools to perform specific quantum computations, such as quantum simulations. As a result, in the last years, quantum simulation has become one of the fields with highest impact inside the quantum information arena.

Trapped ions are one of the most advanced technologies for quantum simulation [6], with widely spread applications, ranging from fermionic lattice models [7] or relativistic quantum mechanics [8] to neural networks [9]. Ions can be efficiently trapped and cooled, their internal states can be precisely manipulated using lasers, with measurements of near unit efficiency [10]. Recently, single-qubit gate fidelities of 99.9999% and two-qubit gates of 99.9% have been achieved [11, 12]. These facts expose that trapped ions is one of the most promising and reliable technologies for quantum simulation protocols.

Spin systems are one of the most studied topics in condensed matter physics. These systems are most commonly used as microscopic models of magnetism, although they are useful in the study of other physical phenomena, such as quantum phase transitions. Many-body spin models are in general intractable once we go beyond 20 spins. Although numerical techniques like DMRG have proven highly useful for computing some spin models, especially the ones with short-range interactions, today the simulation of these models remains as a difficult task. This being the case, we do not exaggerate if we say that the simulation of such quantum spin systems is one of the most interesting applications that a quantum simulator could have. Since the first proposals in trapped ions [13] and in optical lattices [14] a decade ago, the simulation of different spin models has been achieved in different quantum platforms such as the already mentioned ones [15, 16, 17], and recently in superconducting circuits [18].

In this thesis, we will provide with a novel technique for the quantum simulation of spin models in trapped ions, namely the digital-analog approach. This proposed method is a hybrid between the existing analog and digital methods, that aims to overcome the problems that both of these techniques face separately. The thesis contains four chapters:

In chapter 1, we explain the basic concepts of quantum simulation. After presenting the requirements that any quantum simulator must fulfil, we differentiate two types of quantum simulators: digital quantum simulators and analog quantum simulators. In the following sections, we explain the differences between them, and provide insight about the advantages of using one instead of the other.

Chapter 2 is devoted to the exploration of the most interesting one-dimensional spin systems. We focus on different submodes of the Heisenberg model, such as the nearest-neighbor model, the Majumdar-Ghosh model or the Lipkin-Meshkov-Glick model, and review the main features of each model, providing a global view on them.

In chapter 3, we discuss the different interactions that can be implemented in trapped ions. First of all, we present the basic Hamiltonians that appear in a single trapped ion, tuning the laser in different resonances. Later, we generalize to multiple ions, where the Hamiltonians are more complicated. We explain how to generate effective many-body spin-spin interactions such as the Ising or the XY Hamiltonians.

Chapter 4 is the central chapter of this thesis. Using concepts presented in previous chapters, we will propose a quantum simulation of the Heisenberg spin-1/2 chain using a digital-analog approach. For that, we will first introduce the novel concept of digital-analog quantum simulation. And then, we will consider different decompositions of the Heisenberg dynamics in terms of analog blocks, and we will choose the most suitable one. Then, we will compare digital-analog protocols with purely digital approaches. Finally, we will provide numerical simulations of our proposal and we will comment on its main experimental limitations. The thesis closes with a chapter devoted to present the conclusions of the performed investigations.

Chapter 1

Quantum Simulation

Simulating quantum mechanics is a challenging computational problem. The main difficulty is related with the huge amount of computer memory needed to store the quantum state and dynamical evolution of a large quantum system. Being quantum mechanics a probabilistic theory, one needs to compute all possible configurations of the system and their probability amplitudes. Further, the number of parameters needed to characterize a state and its temporal evolution grows exponentially with the system size, which in general is given by the number of degrees of freedom or particles in the system. Although approximation methods like quantum Monte Carlo have helped fighting this difficulty on specific problems, the simulation of large quantum systems remains a hard task even for current supercomputers.

In 1982, Richard Feynman, aware of this problem, proposed to use a computer built of quantum elements -which obey quantum mechanical laws-, instead of the ordinary computers, to simulate quantum systems [1]. Feynman pointed out that this kind of machine would have the capacity to contain an exponentially large amount of information without using an exponentially large amount of physical resources. This led to the envisioning of a new type of computer, the quantum computer, that nowadays promises to do more than simulating quantum mechanics. Although the idea was of great importance, Feynman was not very specific about how this quantum computer was supposed to function. Today it is accepted that a quantum computer should be built by an ensemble of well-defined qubits that can be initialized, measured and on which a universal set of quantum gates can be performed.

In 1996 Seth Lloyd showed that a quantum computer can indeed act as a universal quantum simulator [19]. Universal, in the sense that the same machine, by the use of different algorithms, could be used to simulate very different problems. Analog quantum simulations, however, can be performed using devices substantially more simple than a quantum computer, which are designed to tackle a specific quantum problem. These machines are not universal quantum simulators, but it is expected that this kind of practical quantum simulators will become a reality well before quantum computers. Actually, several research groups are now aiming to realize experiments with tens of qubits, which would be the first practical application in which quantum simulators outperform

classical computers.

In recent years the interest on quantum simulation has been growing rapidly [20, 21], and nowadays quantum simulations are performed in different quantum platforms such as optical lattices, trapped ions or superconducting circuits, among others.

1.1   Requirements for quantum simulators

Quantum simulations consist in the intentional reproduction of the quantum aspects of a physical or unphysical model onto a typically more controllable quantum system. The main elements of controllability are the following [22]:

Quantum system: For the simulation of any quantum system it is necessary to have a certain number of quantum degrees of freedom available in the system. The quantum simulator should be composed by a system of bosons or fermions with or without internal degrees of freedom. Quantum properties are strongly sensitive to environment conditions; in this sense, to control temperature and the size of the system is crucial.

Initialization: To realize the mapping between the two dynamics one has to work in a system that allows the experimentalist to choose its initial state. Usually pure states are the most interesting ones, but to prepare mixed states can be also useful.

Hamiltonian engineering: There must be a correspondence between theoretical interactions we want to simulate and physical operations that we apply to the system. It should be possible to engineer interactions with external fields and among the different particles, with adjustable values. This interaction can be local (acting on neighbouring particles) or long-range.

Detection: Although it is not necessary to be capable of measuring the whole quantum state, we need to perform measurements on the system. The measurement could be individual or collective.

We distinguish two types of quantum simulations: digital quantum simulations and analog quantum simulations

1.2   Digital quantum simulation (DQS)

In digital quantum simulators the evolution operator of the simulated system is implemented by a quantum algorithm constructed by unitary gates. It can be shown that all quantum algorithms can be broken into a sequence of single-qubit operations plus two-qubit operations. This is why quantum computers can perform quantum simulations, and why DQS is universal [19, 23]. Not all mathematically allowed Hamiltonians can be simulated efficiently (with polynomial resources) in this manner. Nevertheless, it is possible to efficiently simulate any finite-dimensional local Hamiltonian, such as local spin systems. In other words, those Hamiltonians that appear in most physical theories

can be simulated efficiently.

As explained before, the unitary evolution of the studied Hamiltonian is broken into a sequence of other unitary gates. However, due to the non-commutativity of quantum mechanics, we generally need to use an approximation while doing this decomposition. Let us suppose that our Hamiltonian can be written as a sum of N terms that describe local interactions

$$H = \sum_{i=1}^{N} H_i. \tag{1.1}$$

If $[H_i, H_j] = 0$ for any i and j, then the unitary evolution as a sequence of local gates is straighforward ($\hbar = 1$)

$$U = e^{-iHt} = \prod_{i=1}^{N} e^{-iH_i t}. \tag{1.2}$$

Unfortunately, in most of the cases of interest $[H_i, H_j] = 0$ does not hold, and we have to make use of the Trotter approximation [24], that states that the dynamics of any Hamiltonian as the one in Eq. (1.1), can be approximated according to the formula

$$e^{-iHt} = (e^{-iH_1 t/l} \cdots e^{-iH_N t/l})^l + \sum_{i<j} \frac{[H_i, H_j]t^2}{2l} + \sum_{k=3}^{\infty} E(k), \tag{1.3}$$

with $\|Ht/l\|_{sup}^{k} l/k!$ being an upper bound on the higher order error terms $E(k)$, where $\|A\|_{sup}$ is the maximum expectation value of the operator A over the states of interest. So if we approximate the unitary evolution as

$$e^{-iHt} \approx (e^{-iH_1 t/l} \cdots e^{-iH_N t/l})^l, \tag{1.4}$$

the total error is less than $\|l(e^{-iHt/l} - 1 + iHt/l)\|_{sup}$, which can be made as small as we want by taking l sufficiently large.

In some cases, we may find interesting to avoid the second-order error term by symmetrizing the Hamiltonian. In the case that we have a Hamiltonian such as $H = H_1 + H_2$, where in principle the Trotterized time evolution would be $U = (e^{-iH_1 t/l} e^{-iH_2 t/l})^l$, symmetrizing the Hamiltonian means to rewrite it like

$$H = \frac{1}{2}H_1 + H_2 + \frac{1}{2}H_1 \tag{1.5}$$

where the Trotterized time evolution is $U \approx (e^{-iH_1 t/2l} e^{-iH_2 t/l} e^{-iH_1 t/2l})^l$.
It can be easily proved that in this case the second-order error term is identically zero. However, note that we have to pay the price of introducing more gates in each Trotter

step. In this very case, where the initial Trotterized evolution contains only two gates, this method is profitable. Although it looks like we have introduced one more gate in each Trotter step, the time evolution can be rewritten as

$$U \approx \left(e^{-iH_1t/2l}e^{-iH_2t/l}e^{-iH_1t/2l}\right)^l = e^{-iH_1t/2l}e^{-iH_2t/l}\left(e^{-iH_1t/l}e^{-iH_2t/l}\right)^{l-1}e^{-iH_1t/2l}, \quad (1.6)$$

where it becomes clear that symmetrizing in this case requires only one more gate in the whole evolution. For the cases in which the initial Trotterized evolution has more than two gates in each Trotter step, this method is not so worthy. This is because in these cases the symmetrization introduces more gates per Trotter step, which can be used to simply enlarge l by doing more (and shorter) Trotter steps.

1.3   Analog quantum simulation (AQS)

In an analog quantum simulation, the Hamiltonian of the simulated system, H_{sys}, is directly mapped onto the Hamiltonian of the simulator, H_{sim}. This last Hamiltonian can to some extent be controlled. As an example we can consider the trapped-ion quantum simulation of the Dirac equation [8, 25]. The Dirac equation in $(1 + 1)$ dimensions for a spin-1/2 particle is

$$i\hbar\frac{\partial}{\partial t}\psi = H_{\mathrm{D}}\psi = (cp\sigma^x + mc^2\sigma^z)\psi \qquad (1.7)$$

where c is the speed of light, m is the rest mass, p is the momentum operator and σ^x and σ^z are the Pauli matrices. The Hamiltonian of a single trapped ion interacting with a bichromatic light field can be written as

$$H_I = 2\eta\Delta\Omega p\sigma^x + \hbar\xi\sigma^z \qquad (1.8)$$

where η is the Lamb-Dicke parameter, Δ is the spatial size of the ground-state wavefunction, and Ω and ξ are parameters tunable with the lasers. Identifying $c \equiv 2\eta\Delta\Omega$ and $mc^2 \equiv \hbar\xi$, H_I has the same mathematical form as H_{D}. Using this analogy, relativistic effects such as *Zitterbewegung* and Klein paradox have been studied in a non-relativistic quantum system [26].

The choice of the mapping depends particularly on the problem to be simulated and the capabilities of the simulator. At first sight, to find a mapping in an AQS might look simpler than to obtain the most efficient gate decomposition for a given Hamiltonian in DQS. Sometimes, like in the previous example, the mapping is indeed straightforward, but frequently suitable mappings have to be designed, introducing external fields or ancillary systems to mediate various interactions.

One of the advantages of AQS is that it could be useful even in the presence of some errors. For example, if we are studying phase transitions in a many-body Hamiltonian, quantitative results may not be so important, and the simulator could be useful to explore

sensitive regions of the system. Regarding the initial state preparation, because of the similarity between the simulated system and the simulator, the preparation process is believed to be more natural than in DQS.

Chapter 2

Spin Systems and the Heisenberg Model

Spin systems are one of the most studied models in physics, and primarily are used to describe magnetism [27]. These systems can either be classical or quantum; in this chapter only the latter type is considered. Particles couple to magnetic fields through their magnetic dipole, just as they couple to electric fields though electric charge. The magnetic dipole of a particle is associated to its spin. Such spin s, carries a magnetic moment of magnitude $\mu = g\mu_{\mathrm{B}}s$, where $\mu_{\mathrm{B}} = \frac{e\hbar}{2mc}$ is the *Bohr magneton* and g the *Landé g factor*. In section 2.1, we will briefly introduce the mathematical form of spin. In section 2.2, we will present different spin systems that are gathered by the general Heisenberg model.

2.1 Spin degree of freedom

The notion that an electron carries an intrinsic half unit of quantum angular momentum $\hbar$ was first proposed by Goudsmit and Uhlenbeck [28]. They needed an extra quantum number to explain the observed atomic expectra and according to them, this could only assume two values, $\pm\hbar/2$. A short time later Dirac [29] deduced this quantization from a vectorial operator that he called *spin*. According to Dirac's theory, spin angular momentum and a point magnetic dipole μ associated with it are inherent properties of the electron.

In quantum mechanics, the spin is described in a Hilbert space of size $2s+1$ and its vectorial operator is given by

$$\vec{S} = S^x\hat{\imath} + S^y\hat{\jmath} + S^z\hat{k} = (S^x, S^y, S^z). \tag{2.1}$$

In the most elementary case, where $s = \frac{1}{2}$, this is expressed as

$$\vec{S} = \frac{\hbar}{2}(\sigma^x, \sigma^y, \sigma^z) \tag{2.2}$$

where σ^x,σ^y and σ^z are Pauli matrices typically defined as

$$\sigma^x = \begin{pmatrix} 0 & 1 \\ 1 & 0 \end{pmatrix} \quad \sigma^y = \begin{pmatrix} 0 & -i \\ i & 0 \end{pmatrix} \quad \sigma^z = \begin{pmatrix} 1 & 0 \\ 0 & -1 \end{pmatrix}. \tag{2.3}$$

Quantum spin-1/2 states are described by *spinors*, which can be represented as

$$\Psi = \begin{pmatrix} \alpha \\ \beta \end{pmatrix} = \alpha|\uparrow\rangle + \beta|\downarrow\rangle \tag{2.4}$$

where α and β are complex numbers and the up-state $|\uparrow\rangle$ and down-state $|\downarrow\rangle$ are eigenvectors of σ^z.

2.2 Spin systems

Spin models are used to describe basically magnetic dipole-dipole interactions in magnetic systems, but can also be useful to describe quantum phase transitions or superconductivity. Most of one-dimensional spin models can in general be described by the XYZ anisotropic spin chain, which Hamiltonian can be written

$$H_{\text{XYZ}} = \sum_{i<j} J_{ij}^x S_i^x S_j^x + J_{ij}^y S_i^y S_j^y + J_{ij}^z S_i^z S_j^z, \tag{2.5}$$

Typically, the isotropic model is considered, which is called the Heisenberg model. The Heisenberg model is central to the theory of spin systems and it gathers several spin models, as the Lipkin-Meskov-Glick model, Majumdar-Ghosh model, Haldane-Shastri model or Nearest-Neighbours model. In general the Heisenberg model describes a system of N particles that have a spin-spin interaction. The general isotropic Heisenberg Hamiltonian has form

$$H_{\text{HB}} = \sum_{i<j}^{N} J_{ij} \ \vec{S}_i \cdot \vec{S}_j \tag{2.6}$$

where $\sum_{i<j} \equiv \sum_{i=1}^{N-1} \sum_{j=i+1}^{N}$, $\vec{S}_i$ is a vector representing the spin of the i-th particle, and J_{ij} its interaction with the j-th particle. In general, we look for solutions that diagonalize the Hamiltonian. Unfortunately, this is only possible for a particular type of interactions J_{ij}. However, we can study some general properties of the system looking for the symmetries of the Hamiltonian.

We will now discuss several properties of the general Heisenberg model and then describe the different spin models contained in it.

2.2.1 Symmetries and conserved quantities

In this chapter we will review the main symmetries of the general Heisenberg Hamiltonian. Let us consider first the operator
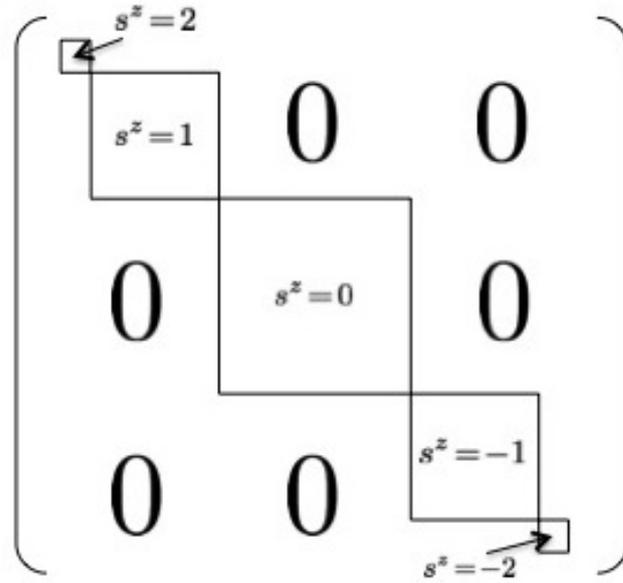
$$S^z = \sum_i S_i^z, \tag{2.7}$$

Figure 2.1: Matrix representation of a spin-1/2 Heiseberg model for $N = 4$ spins.

which measures the magnetization. We can check that it commutes with the Hamiltonian, $[H_{\mathrm{HB}}, S^z] = 0$. This basically means that if a state is an eigenstate of S^z with eigenvalue s^z, the action of the Heisenberg Hamiltonian on this state will never change the value of s^z. In other words, s^z is a conserved quantity. When the exact diagonalization of the Hamiltonian is not possible, conserved quantities and symmetries can help us to split the total Hilbert space of the problem in different subspaces. In this case, different values for s^z characterize different subspaces.

In Fig. 2.1, we can see a matrix representation of a general spin-1/2 Heisenberg Hamiltonian for $N = 4$. The $2^4 \times 2^4$ matrix has been considerably reduced to 5 smaller submatrices. Predicting the size of these submatrices is simple. If $|\uparrow\rangle$ and $|\downarrow\rangle$ are the up and down states, where $S^z|\uparrow\rangle = \frac{\hbar}{2}|\uparrow\rangle$ and $S^z|\downarrow\rangle = -\frac{\hbar}{2}|\downarrow\rangle$, $|\uparrow\uparrow\uparrow\uparrow\rangle$ is the only possible state for obtaining $s^z = 2$ (1×1). At the same time, to obtain $s^z = 1$, we have four (4×4) possible combinations, which are orthogonal to each other, namely $|\downarrow\uparrow\uparrow\uparrow\rangle$, $|\uparrow\downarrow\uparrow\uparrow\rangle$, $|\uparrow\uparrow\downarrow\uparrow\rangle$, and $|\uparrow\uparrow\uparrow\downarrow\rangle$.

There is also an interesting feature of the spin-1/2 Heisenberg model that is general for any kind of spin-spin coupling J_{ij}. The $|\uparrow\uparrow\cdots\uparrow\rangle$ and $|\downarrow\downarrow\cdots\downarrow\rangle$ states are always eigenstates of the Hamiltonian. In the ferromagnetic cases ($J_{ij} < 0$), these states belong to the subspace of degenerate lower eigenvalue.

2.2.2   Nearest-neighbour (NN) model

The nearest-neighbour (NN) Heisenberg model describes a linear array of spin-1/2 particles with a uniform exchange interaction between nearest-neighbours. The associated Hamiltonian reads

$$H_{\text{NN}} = -J \sum_{i=1}^{N} \vec{S}_i \cdot \vec{S}_{i+1}, \tag{2.8}$$

where, in this case, we assume $J_{ij} = -J$ if $j = i+1$ and $J_{ij} = 0$ elsewhere, and periodic boundary conditions $\vec{S}_{N+1} = \vec{S}_1$. In 1931 Hans Bethe presented a method for obtaining the exact eigenvalues and eigenfunctions of this model [30]. The method is known by *Bethe ansatz*. The Hamiltonian in Eq. (2.8) can be rewritten in the following form,

$$H_{\text{NN}} = -J \sum_{i=1}^{N} \big[\tfrac{1}{2}(S_i^+ S_{i+1}^- + S_i^- S_{i+1}^+) + S_i^z S_{i+1}^z \big]. \tag{2.9}$$

As we have exposed in the previous section, the rotational symmetry around the z-axis implies that the total spin S^z is conserved. We will define $r = N/2 - S^z$ as the number of down spins, and each r will delimit a block just as in Fig. 2.1.
The block with $r = 0$ (all spins up) consists of a single vector $|F\rangle \equiv \|\uparrow \dots \uparrow\rangle$, which is an eigenstate of the Hamiltonian $H_{\text{NN}}|F\rangle = E_0|F\rangle$, with energy $E_0 = -JN/4$.

One-magnon excitations: In an elastic solid, the oscillations of atoms are ruled by their normal modes. In quantum mechanics, we quantize the amplitude of the individual normal modes into units known as *phonons*. The analogous of normal modes in the magnetic systems are spin waves; when we quantize them, the basic unit is defined as *magnon*. The N vectors that form the block $r = 1$ are labeled by the position of the flipped spin

$$|n\rangle = S_n^-|F\rangle \qquad n = 1, \dots, N. \tag{2.10}$$

To diagonalize the $r = 1$ block, which has size $N \times N$, we take into account the invariance of H_{NN} with respect to discrete translations by any number of lattice spacings. We construct translationally invariant basis vectors by writing

$$|\psi_k\rangle = \frac{1}{\sqrt{N}} \sum_{n=1}^{N} e^{ikn}|n\rangle, \tag{2.11}$$

which are eigenvectors of the translation operator with eigenvalue e^{ik} for $k = 2\pi m/N$, $m = 0, \dots, N-1$. For a vector $|n\rangle$, the action of the translation operator means $T|n\rangle = |n-1\rangle$, and with periodic boundary conditions, $T|1\rangle = |N\rangle$. For $N = 3$,

$$T|\psi_k\rangle = \frac{1}{\sqrt{3}} T(|1\rangle + e^{ik}|2\rangle + e^{i2k}|3\rangle) = e^{ik} \frac{1}{\sqrt{3}}(e^{-ik}|3\rangle + |1\rangle + e^{ik}|2\rangle) \tag{2.12}$$

and if we impose that $e^{-ik} = e^{i2k}$, thus $k = \frac{2\pi}{3}m$, we obtain $T|\psi_k\rangle = e^{ik}|\psi_k\rangle$.
The vectors $|\psi_k\rangle$ are also eigenvectors of the Hamiltonian H_{NN} with eigenvalues

$$E = J(1 - \cos k) + E_0. \tag{2.13}$$

Notice that there is no gap between the ground state and the first excited state. Vectors $|\psi_k\rangle$ represent one-magnon excitations with wave vector k. Using Bethe ansatz, it is possible to compute also two-magnon excitations [31].

2.2.3 J_1-J_2 model / Majumdar-Ghosh (MG) model

The Heisenberg model with nearest-neighbour and next-nearest-neighbor (NNN) inter-actions, J_1 and J_2 is in general called J_1-J_2 model. When $J_2 = 0.5J_1$, the model is called Majumdar-Ghosh (MG) [32], and the Hamiltonian is given by

$$H_{\mathrm{MG}} = J \sum_{i=1}^{N} \vec{S}_i \cdot \vec{S}_{i+1} + \frac{J}{2} \sum_{i=1}^{N} \vec{S}_i \cdot \vec{S}_{i+2}. \tag{2.14}$$

This model is solvable and in the case of periodic boundary conditions, and N even, the ground states are $|\Psi_+\rangle$ and $|\Psi_-\rangle$ [33]

$$|\Psi_\pm\rangle = \prod_{i=1}^{N/2} (|\uparrow\downarrow\rangle_{2i,2i\pm1} - |\downarrow\uparrow\rangle_{2i,2i\pm1})/\sqrt{2} \tag{2.15}$$

As we may notice, the state is a product of singlets; these states are called *dimer* states. In these states, a spin is fully correlated with one nearest neighbour, and fully uncorre-lated with the other spins. In the case of open boundary conditions, the ground state is only given by $|\Psi_-\rangle$.

When $J_2/J_1 \cong 1/4$, it is known that the model shows a *dimerization transition* and this transition is studied in the context of the anisotropic XXZ chain with NNN interactions [34, 35]. The general Hamiltonian can be written

$$H = \sum_{i=1}^{N}(S_i^x S_{i+1}^x + S_i^y S_{i+1}^y + \Delta S_i^z S_{i+1}^z) + \alpha \sum_{i=1}^{N}(S_i^x S_{i+2}^x + S_i^y S_{i+2}^y + \Delta S_i^z S_{i+2}^z), \tag{2.16}$$

where $\alpha = J_2/J_1$, and we assume periodic boundary conditions. Critical points are determined using level crossing of first excited states; these crossings delimit different regions. In Fig. 2.2 different regions are shown, depending on α and Δ.

2.2.4   Lipkin-Meshkov-Glick (LMG) model

In this section, we will introduce briefly the Lipkin-Meshkov-Glick (LMG) model [36], which is the long-range limiting case of the Heisenberg Hamiltonian, where interactions are spatially independent, that is, $J_{ij} = J$. In this case, the Heisenberg Hamiltonian can be rewritten as

$$H_{\mathrm{LMG}} = \frac{J}{2}(\mathbf{S}^2 - \sum_{i=1}^{N} \mathbf{S}_i^2). \tag{2.17}$$
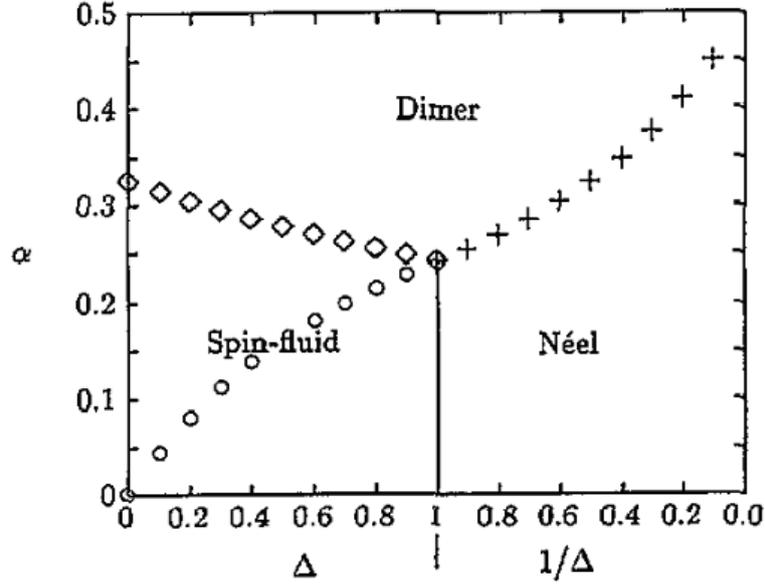
Figure 2.2: Different regions showing regimes of the antiferromagnetic XXZ chain with NNN interactions [35].

The Hamiltonian can be analytically diagonalized and is a common exercise of quantum mechanics textbooks. For the spin-1/2 $N = 3$ case, for example, the basis of eigenstates is given by the following operators: $\{\mathbf{S}^2, \mathbf{S}_{12}^2, S^z, \mathbf{S}_1^2, \mathbf{S}_2^2, \mathbf{S}_3^2\}$, where $\mathbf{S} = (\mathbf{S}_1 + \mathbf{S}_2 + \mathbf{S}_3)$ and $\mathbf{S}_{12} = (\mathbf{S}_1 + \mathbf{S}_2)$. The state $|s_{12}, j, s^z\rangle$ is an eigenstate of the Hamiltonian and can be related with the typical products of up and down states using *Clebsch-Gordan coefficients*, which are introduced in the theory of angular-momentum addition. For this trivial case, where the energy is $E = J/2(j(j + 1) - 9/4)$, the eigenstates of the Hamiltonian are

$$
\begin{aligned}
s_{12} = 1; j = 3/2 &\left\{ \begin{array}{l}
|1, 3/2,\ 3/2\rangle = |\uparrow\uparrow\uparrow\rangle \\
|1, 3/2,\ 1/2\rangle = \frac{1}{\sqrt{3}}(|\uparrow\uparrow\downarrow\rangle + |\uparrow\downarrow\uparrow\rangle + |\downarrow\uparrow\uparrow\rangle) \\
|1, 3/2, -1/2\rangle = \frac{1}{\sqrt{3}}(|\uparrow\downarrow\downarrow\rangle + |\downarrow\uparrow\downarrow\rangle + |\downarrow\downarrow\uparrow\rangle) \\
|1, 3/2, -3/2\rangle = |\downarrow\downarrow\downarrow\rangle
\end{array} \right\} \\
s_{12} = 1; j = 1/2 &\left\{ \begin{array}{l}
|1, 1/2, 1/2\rangle = \frac{1}{\sqrt{6}}(2|\uparrow\uparrow\downarrow\rangle + |\uparrow\downarrow\uparrow\rangle + |\downarrow\uparrow\uparrow\rangle) \\
|1, 1/2, -1/2\rangle = \frac{1}{\sqrt{6}}(|\uparrow\downarrow\downarrow\rangle + |\downarrow\uparrow\downarrow\rangle + 2|\downarrow\downarrow\uparrow\rangle)
\end{array} \right\} \\
s_{12} = 0; j = 1/2 &\left\{ \begin{array}{l}
|0, 1/2, 1/2\rangle = \frac{1}{\sqrt{2}}(|\uparrow\downarrow\uparrow\rangle - |\downarrow\uparrow\uparrow\rangle) \\
|0, 1/2, -1/2\rangle = \frac{1}{\sqrt{2}}(|\uparrow\downarrow\downarrow\rangle - |\downarrow\uparrow\downarrow\rangle)
\end{array} \right\}
\end{aligned}
\tag{2.18}
$$

For a general number of spins N_s, the problem becomes difficult to treat in the paper, but some general results are known. For the antiferromagnet, any singlet state is

a ground state, which leads to a huge degeneracy. The number of singlet states that we can find with N_s spin-1/2 particles is given by the Catalan number

$$C_n = \frac{N!}{(\frac{N}{2})!(\frac{N}{2}+1)!}.$$ (2.19)

In the ferromagnet $(J < 0)$, the ground states are symmetric Dicke states, like the ones that we see in the example above, and its degeneracy is given by $(N + 1)$.

Chapter 3

Trapped Ions

Trapped-ion systems are one of the most promising technologies for quantum simulations [6]. Ions are trapped using combinations of electrostatic and magnetic fields (Penning trap) or a spatially varying time-dependent electromagnetic field, usually in the radio-frequency domain (Paul traps). In this work, only the latter type will be considered. Typically, two metastable electronic levels are use as a quantum two-level system or qubit [10]. Using sideband cooling, it is possible to cool down the ionic motional degrees of freedom to their ground state, and treat them as quantum harmonic oscillators. This motion of the ions can be also used to generate effective interactions among them.

3.1 Single trapped ion

Single trapped ions represent elementary quantum systems that are isolated from the environment. As we mentioned before, the internal electronic structure of an ion confined in a linear Paul trap can be approximated by a two-level system, being $|g\rangle$ and $|e\rangle$ the ground and excited states, respectively, and the energy difference $\hbar\omega_0 = \hbar(\omega_e - \omega_g)$. According to that, the two-level Hamiltonian is

$$H_q = \hbar\omega_g|g\rangle\langle g| + \hbar\omega_e|e\rangle\langle e|. \tag{3.1}$$

This can be written also as

$$H_q = \frac{\hbar\omega_0}{2}(|e\rangle\langle e| - |g\rangle\langle g|) + \hbar\frac{\omega_e + \omega_g}{2}(|e\rangle\langle e| + |g\rangle\langle g|). \tag{3.2}$$

Any operator related to a two-level system can be expressed using the spin-1/2 algebra, since the three Pauli matrices and I, the 2×2 identity matrix, span the full vector space of 2×2 Hermitian matrices. In the particular case at hand the mapping is

$$|e\rangle\langle e| + |g\rangle\langle g| \longrightarrow I = \begin{pmatrix} 1 & 0 \\ 0 & 1 \end{pmatrix}, \qquad |e\rangle\langle g| \longrightarrow \sigma^+ = \begin{pmatrix} 0 & 1 \\ 0 & 0 \end{pmatrix},$$

$$|g\rangle\langle e| \longrightarrow \sigma^- = \begin{pmatrix} 0 & 0 \\ 1 & 0 \end{pmatrix}, \qquad |e\rangle\langle e| - |g\rangle\langle g| \longrightarrow \sigma^z = \begin{pmatrix} 1 & 0 \\ 0 & -1 \end{pmatrix} \tag{3.3}$$

where,

$$|e\rangle \rightarrow \begin{pmatrix} 1 \\ 0 \end{pmatrix} \quad |g\rangle \rightarrow \begin{pmatrix} 0 \\ 1 \end{pmatrix}. \tag{3.4}$$

With this mapping the two-level Hamiltonian is reexpressed as

$$H_{\mathrm{q}} = \frac{\hbar\omega_0}{2}\sigma^z, \tag{3.5}$$

where the energy is rescaled by $-\hbar(\omega_{\mathrm{e}} + \omega_{\mathrm{g}})/2$ to suppress the state-independent energy contribution in Eq. (3.2).

The quantum mechanical motion of the ion is typically modelled as a quantum harmonic oscillator $\hbar\nu a^\dagger a$, where $a(a^\dagger)$ is the annihilation(creation) operator of the motional degree of freedom and ν is the trap frequency on the direction of this motion. The coupling to a light field is described by the following Hamiltonian

$$H = \frac{\hbar\omega_0}{2}\sigma^z + \hbar\nu a^\dagger a + \frac{\hbar\Omega}{2}\sigma^x \cos\left(kx - \omega_L t + \phi_L\right) \tag{3.6}$$

where ω_L is the frequency of the driving laser field, k is the laser wave vector, ϕ_L is the laser phase, and Ω is the Rabi frequency associated with the atom-laser coupling strength. For simplicity, the discussion will be restricted to one dimension where the wave vector $\vec{k}$ is chosen to lie along the x axis of the trap. To extend the description to more dimensions is straightforward.

   To visualize the dynamics induced by the light field, we need to go to an interaction picture characterized by the free Hamiltonian $H_0 = \frac{\hbar\omega_0}{2}\sigma^z + \hbar\nu a^\dagger a$. The Hamiltonian in the interaction picture is given by

$$H^I = e^{i(\frac{\omega_0}{2}\sigma^z + \nu a^\dagger a)t}\frac{\hbar\Omega}{2}(\sigma^+ + \sigma^-)(e^{i(kx - \omega_L t + \phi_L)} + e^{-i(kx - \omega_L t + \phi_L)})e^{-i(\frac{\omega_0}{2}\sigma^z + \nu a^\dagger a)t}. \tag{3.7}$$

By using the Baker-Campbell-Hausdorff formula,

$$e^{iG\lambda}Ae^{-iG\lambda} = A + i\lambda[G, A] + \frac{(i\lambda)^2}{2!}[G, [G, A]] + ..., \tag{3.8}$$

and commutation relations $[\sigma^+, \sigma^z] = -2\sigma^+$, $[\sigma^-, \sigma^z] = 2\sigma_-$, $[a^\dagger a, a^\dagger] = a^\dagger$ and $[a^\dagger a, a] = -a$, it can be proven, after some mathematically involved calculus, that this Hamiltonian is equivalent to

$$H^I = \frac{\hbar\Omega}{2}(\sigma^+ e^{i\omega_0 t} + \sigma^- e^{-i\omega_0 t})(e^{i(\eta(e^{i\nu t}a^\dagger + e^{-i\nu t}a) - \omega_L t + \phi_L)} + e^{-i(\eta(e^{i\nu t}a^\dagger + e^{-i\nu t}a) - \omega_L t + \phi_L)}), \tag{3.9}$$

where $\eta \equiv k\sqrt{\frac{\hbar}{2M\nu}}$ is called the Lamb-Dicke parameter. This Hamiltonian can be seen as the sum of four terms, each of them multiplied by terms like $e^{\pm i(\omega_L \pm \omega_0)t}$. The laser frequency ω_L is chosen to be almost in resonance with the electronic transition, in a way

that $\epsilon \equiv \omega_L - \omega_0 \ll \omega_L + \omega_0$. Along with this, if the Rabi frequency is also much smaller than ω_0, $\Omega \ll \omega_0$, the rapidly oscillating terms (those with $\omega_L + \omega_0$) have a negligible contribution in the time evolution, and they can be removed from the Hamiltonian. Doing so is called the *optical rotating-wave approximation* and leads to the following Hamiltonian

$$H^I = \frac{\hbar\Omega}{2}\sigma^+ \exp\left\{i\eta(e^{i\nu t}a^\dagger + e^{-i\nu t}a)\right\}e^{-i(\epsilon t - \phi_L)} + \text{H.c.} \tag{3.10}$$

The interaction Hamiltonian in Eq. (3.9) can be simplified if we consider the ion confined in the Lamb-Dicke regime, where the extension of the ion wave function is much smaller than the laser wavelength. In this regime, the condition $\eta\sqrt{\langle(a+a^\dagger)^2\rangle} \ll 1$ must hold for all times. Once we have this condition, we can expand the exponential to the lowest order in η and we obtain the Lamb-Dicke Hamiltonian for a single trapped ion,

$$H_{\text{LD}} = \frac{\hbar\Omega}{2}\sigma^+\{1 + i\eta(e^{i\nu t}a^\dagger + e^{-i\nu t}a)\}e^{-i(\epsilon t - \phi_L)} + \text{H.c.} \tag{3.11}$$

This Hamiltonian, in different resonances, will provide us with all the essential interactions that take place in a single trapped ion.

3.1.1 Single-spin rotations

Spin or qubit rotations can be performed if we tune the laser into the *carrier resonance*. In Eq. (3.11), this corresponds to choosing $\epsilon = 0$. Under a second rotating-wave approximation (RWA), called this time *vibrational* RWA, we can neglect terms oscillating with frequencies of the order of ν, and the effective Hamiltonian reads

$$H^{\text{car}} = \frac{\hbar\Omega}{2}(\sigma^+ e^{i\phi_L} + \sigma^- e^{-i\phi_L}). \tag{3.12}$$

Note that this Hamiltonian does not involve the motional degrees of freedom. The effect of a pulse of such resonant radiation is well described by a rotation $R(\theta, \varphi)$ acting on the spin state,

$$R(\theta, \varphi) = \exp\left(i\theta/2(\sigma_+ e^{i\varphi} + \sigma_- e^{-i\varphi})\right) = I\cos\theta/2 + i(\sigma^x\cos\varphi - \sigma^y\sin\varphi)\sin\theta/2, \tag{3.13}$$

where $\varphi = \phi_L + \pi$ and $\theta = \Omega t$. More conveniently, the qubit rotation $R(\theta, \varphi)$ is written using Pauli-spin matrices as

$$R(\theta, \varphi) = \begin{pmatrix} \cos\theta/2 & ie^{i\varphi}\sin\theta/2 \\ ie^{-i\varphi}\sin\theta/2 & \cos\theta/2 \end{pmatrix}. \tag{3.14}$$

Qubit or spin-1/2 rotations can be visualized using the so-called Bloch sphere. We identify the north pole of the Bloch sphere with the up state $|\uparrow\rangle$ and the south pole with the down state $|\downarrow\rangle$ (see Fig. 3.1). In the Bloch picture, the angle φ specifies the axis of
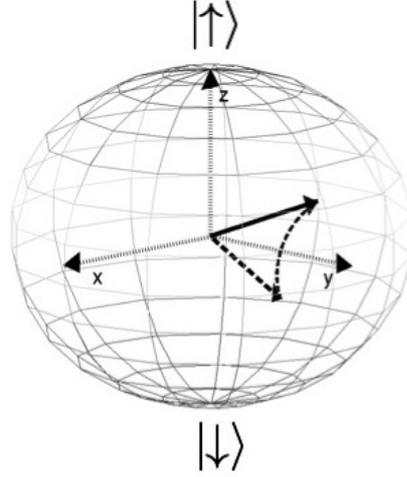
Figure 3.1: Rotation around the y axis visualized on the Bloch sphere [6].

rotation in the equatorial plane, thereby, $\varphi = 0$ and $\varphi = \pi/2$ correspond to rotations around the x $(R_x(\theta) \equiv R(\theta, 0))$ and y $(R_x(\theta) \equiv R(\theta, \pi/2))$ axis, respectively.

Rotations around the z axis can be always decomposed into rotations around x and y axis. However, there is also an alternative way to perform such rotations, consisting in the use of a *detuned carrier* interaction, which is obtained by taking $\epsilon = -\Delta$, and $|\Delta| \ll |\nu|$ and its Hamiltonian reads

$$H^{\mathrm{d/car}} = \frac{\hbar\Omega}{2}(\sigma^+ e^{i\phi}e^{i\Delta t} + \sigma^- e^{-i\phi}e^{-i\Delta t}). \tag{3.15}$$

Although this Hamiltonian looks quite simple, its time evolution is not. The evolution of any time-dependent Hamiltonian is given by the time-ordered exponential of the Hamiltonian integral between times t_0 and t

$$U(t, t_0) = \mathcal{T}(e^{-\frac{i}{\hbar}\int_{t_0}^t dt' H(t')}) \tag{3.16}$$

when the H's at different times do not commute, the time ordering is not trivial and can be approximated using Dyson series or alternatively the Magnus expansion. Using the latter, the time evolution operator for a time t is given by

$$U(t, 0) = e^{\Omega_1(t) + \Omega_2(t) + \cdots} \tag{3.17}$$

where

$$\Omega_1(t) = -\frac{i}{\hbar} \int_0^t \mathrm{d}t' \ H(t')$$

$$\Omega_2(t) = -\frac{1}{2\hbar^2} \int_0^t \mathrm{d}t_1 \int_0^{t_1} \mathrm{d}t_2 \ [H(t_1), H(t_2)]. \tag{3.18}$$

For the moment, we will consider only the first and second terms of the expansion. The first order term is the one that we are most familiar with. The commutator on the second order term is given in our case by

$$[H(t_1), H(t_2)] = \frac{\hbar^2 \Omega^2}{4}[\sigma^+ e^{i\phi} e^{i\Delta t_1} + \sigma^- e^{-i\phi} e^{-i\Delta t_1}, \sigma^+ e^{i\phi} e^{i\Delta t_2} + \sigma^- e^{-i\phi} e^{-i\Delta t_2}], \quad (3.19)$$

which can be simplified using the commutation relation $[\sigma^+, \sigma^-] = \sigma^z$ to

$$[H(t_1), H(t_2)] = i\frac{\hbar^2 \Omega^2}{2}\sigma^z \sin \Delta(t_2 - t_1). \quad (3.20)$$

Solving the first integral, the second-order term reads

$$\Omega_2(t) = \int_0^t dt_1 \frac{i\Omega^2}{4}\sigma^z \int_0^{t_1} dt_2 \sin \Delta(t_2 - t_1) = \int_0^t dt_1 \frac{i\Omega^2}{4\Delta}\sigma^z(1 - \cos \Delta t_1). \quad (3.21)$$

We can consider the contribution of Ω_1 and Ω_2 in a single integral

$$\Omega_1(t) + \Omega_2(t) = -i\int_0^t dt_1 \{\Omega(\sigma^+ e^{i\phi} e^{i\Delta t_1} + \sigma^- e^{-i\phi} e^{-i\Delta t_1}) - \frac{\Omega^2}{4\Delta}\sigma^z(1 - \cos \Delta t_1)\}. \quad (3.22)$$

At this point, we are going to apply a rotating-wave-like approximation and neglect all the terms that depend on t_1. Assuming that Ω_3 and higher order terms are also negligible ($\Omega^2/\Delta^2 \ll 1$), the evolution is given only by

$$U(t, 0) = e^{i\frac{\Omega^2}{4\Delta}\sigma^z}. \quad (3.23)$$

So we conclude that the evolution that is produced by the detuned carrier interaction corresponds to the dynamics of an effective Hamiltonian of the form

$$H_{\text{eff}} = -\frac{\hbar\tilde{\Omega}}{2}\sigma^z \quad (3.24)$$

with an effective Rabi frequency $\tilde{\Omega} = \Omega^2/2\Delta$.

In this way, rotations around the z-axis can be implemented directly, without decomposing them into two rotations. These kind of qubit rotations can be written also using Pauli matrices as

$$R_z(\tilde{\theta}) = \begin{pmatrix} e^{i\tilde{\theta}/2} & 0 \\ 0 & e^{-i\tilde{\theta}/2} \end{pmatrix}, \quad (3.25)$$

where $\tilde{\theta} = \tilde{\Omega}t$. Finally, notice that the obtained effective Hamiltonian is independent of the laser phase ϕ_L. This feature makes this last gate robust against any fluctuations that this phase may suffer.

3.1.2 Jaynes-Cummings interaction

If we consider now the Lamb-Dicke Hamiltonian of Eq. (3.11), we choose $\epsilon = -\nu$ and apply the vibrational RWA, the effective Hamiltonian that is left has the form

$$H^{\text{rsb}} = \hbar\Omega i\eta(a\sigma^+ e^{i\phi_L} - a^\dagger \sigma^- e^{-i\phi_L}). \tag{3.26}$$

This resonance is known as *first red sideband*. As it is clear from the Hamiltonian, this resonance couples the internal levels of the ion with the quantized motional mode. This Hamiltonian is known as the Jaynes-Cummings Hamiltonian, which is a theoretical model that describes the interaction between a two-level atom and the quantized light field in an optical cavity. In this case, the quantized motion of the ion acts as the light-field in the original model.

If we have the initial state $|g, n\rangle$, it can be proven that the evolution is given by

$$|n, \text{g}\rangle \;\rightarrow\; \cos\big(\frac{\Omega t}{2}\sqrt{n}\big)|n, \text{g}\rangle + e^{i\phi_L}\sin\big(\frac{\Omega t}{2}\sqrt{n}\big)|n-1, \text{e}\rangle. \tag{3.27}$$

From this evolution, we see that the *first red sideband* Hamiltonian gives rise to transitions of the type $|n, \text{g}\rangle \leftrightarrow |n-1, \text{e}\rangle$, with Rabi frequency $\Omega_{n,n-1} = \eta\Omega\sqrt{n}$. Measuring the internal state of the ion we are able to know also the motional state, because of the entanglement property between them. This entanglement property of the Jaynes-Cummings Hamiltonian makes this model one of the most appropriate to study the basic properties of quantum correlations.

We can do a similar thing by taking $\epsilon = \nu$ in the Lamb-Dicke Hamiltonian. The resultant effective Hamiltonian is

$$H^{\text{bsb}} = \hbar\Omega i\eta(a^\dagger \sigma^+ e^{i\phi_L} - a\sigma^- e^{-i\phi_L}). \tag{3.28}$$

This resonance is known as the *first blue sideband* and the effective Hamiltonian as the anti-James-Cummings Hamiltonian. While the Jaynes-Cummings Hamiltonian produces transitions of the type $|n, \text{g}\rangle \leftrightarrow |\text{n}-1, \text{e}\rangle$, the anti-Jaynes-Cummings Hamiltonian produces transitions of the type $|n, \text{g}\rangle \leftrightarrow |\text{e}, n+1\rangle$. The exact expression for the evolution of the initial state $|n, g\rangle$ is given by

$$|n, \text{g}\rangle \;\rightarrow\; \cos\big(\frac{\Omega t}{2}\sqrt{n+1}\big)|n, \text{g}\rangle + e^{i\phi_L}\sin\big(\frac{\Omega t}{2}\sqrt{n+1}\big)|n+1, \text{e}\rangle, \tag{3.29}$$

where the Rabi frequency is $\Omega_{n,n+1} = \eta\Omega\sqrt{n+1}$.

One may be interested in driving the presented interactions as fast as possible. To speed up the quantum operations, we need to increase the value of the Rabi frequency Ω. However, we have to take into account the fact that the vibrational RWA does not hold for Rabi frequencies comparable with the trap frequencies ν, especially for small Lamb-Dicke factors.
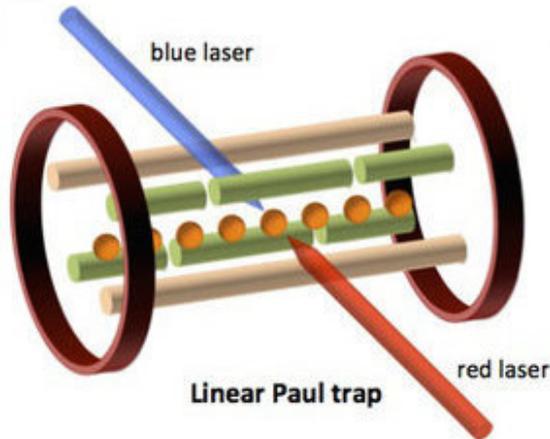
Figure 3.2: Multiple ions in a linear Paul trap [37].

3.2   Multiple ion chain

When we introduce more than one ion in a linear trap, Coulomb repulsion terms appear and the ions are ordered forming a string or chain along the longitudinal axis (z) or the trap. For that, the trapping force in this direction has to be weaker. Coulomb repulsion is balanced with the trapping forces and as a result each ion occupies an equilibrium position z_i^0.

Typically, all the ions are coupled to the same laser field; we call this *global addressing*. Thereby, all concepts of the previous section are extended to the multiple ion case without much complication. If we tune the laser in the carrier transition, we will produce all the qubits (spins) to rotate in the same way simultaneously i.e. global spin rotations. It is also possible to act on each ion individually; this is known as *individual addressing*. However, this is in general much more difficult to implement in experiments.

In this section, we will present the details of the engineering of many body spin-spin interactions like the Ising or XY models, recently implemented in several experiments [38, 39, 40, 41]. This effective interactions are actually mediated by collective vibrational modes of the ion chain. N ions have N normal modes in each direction. The general Hamiltonian of N ions coupled to a light field in a Paul trap can be written as

$$H = \sum_i \frac{\hbar\omega_0}{2}\sigma_i^z + \sum_{\alpha,m} \hbar\nu_{\alpha,m} a_{\alpha,m}^\dagger a_{\alpha,m} + \sum_i \frac{\hbar\Omega_i}{2}\sigma_i^x \cos\left(\vec{k}\cdot\vec{x_i} - \omega_L t + \phi_L\right) \qquad (3.30)$$

where $\nu_{\alpha,m}$ is the vibrational frequency of the m-th mode in the α direction, $\vec{k}$ is the wave vector of the laser field and x_i is the position of the i-th ion. We are going to take the laser lying in a direction perpendicular to the longitudinal (z) axis, in this way, we will only care about the radial directions (x and y), that will give rise to $2N$ radial modes.

In the case of a single ion, the position of the ion was quantized $x = \sqrt{\hbar/2M\nu}(a + a^\dagger)$, nevertheless, in the case of an ion string the quantized operators are the normal modes Q_m and the position of each ion in terms of the modes is given by [42] [43]

$$
\begin{aligned}
x_i &= \sum_{m=1}^{N} \mathcal{M}_{i,m}^x Q_m^x = \sum_{m=1}^{N} \sqrt{\frac{\hbar}{2M\nu_m^x}} \mathcal{M}_{i,m}^x (a_{x,m} + a_{x,m}^\dagger) \\
y_i &= \sum_{m=1}^{N} \mathcal{M}_{i,m}^y Q_m^y = \sum_{m=1}^{N} \sqrt{\frac{\hbar}{2M\nu_m^y}} \mathcal{M}_{i,m}^y (a_{y,m} + a_{y,m}^\dagger)
\end{aligned}
\tag{3.31}
$$

where $\mathcal{M}_{i,m}^x$ and $\mathcal{M}_{i,m}^y$ are the normal mode transformation matrices in the x and y directions, and M is the mass of the ion. Using the relations given above, the Hamiltonian equivalent to the one in Eq. (3.9) for N ions is

$$
H^I = \sum_{i=1}^{N} \frac{\hbar\Omega_i}{2} \sigma_i^+ \exp\left\{ i \sum_{m=1}^{2N} \eta_{i,m}(e^{i\nu_m t}a_m^\dagger + e^{-i\nu_m t}a_m) \right\} e^{-i(\epsilon t - \phi_L)} + \text{H.c.},
\tag{3.32}
$$

where we have considered on a single sum the modes for the x and y directions, and the Lamb-Dicke parameter that relates the i-th ion with the m-th normal mode reads

$$
\eta_{i,m} = \mathcal{M}_{i,m}\Delta k \sqrt{\frac{\hbar}{2M\nu_m}}.
\tag{3.33}
$$

If we now consider the Lamb-Dicke regime, the resulting Hamiltonian provides us with the necessary tools to engineer effective spin-spin interactions in trapped ions.

3.2.1   Effective spin-spin interactions

The interaction Hamiltonian of an ion chain coupled to a transverse laser field in the Lamb-Dicke regime $(\eta_{i,m}\sqrt{\langle (a_m + a_m^\dagger)^2 \rangle} \ll 1)$ is given by

$$
H_{\text{LD}} = \sum_{i=1}^{N} \frac{\hbar}{2}\Omega_i \sigma_i^+ \left\{ 1 + \sum_{m=1}^{2N} i\eta_{i,m}(a_m e^{-i\nu_m t} + a_m^\dagger e^{i\nu_m t}) \right\} e^{i(-\epsilon t + \phi)} + \text{H.c.},
\tag{3.34}
$$

where ν_m is the m-th mode frequency and $\epsilon = \omega_L - \omega_0$ is the difference between the laser and the carrier frequency. We will employ a bichromatic laser with beatnote frequencies $\epsilon = \pm(\nu_{\text{CM}} + \Delta) + \delta$, where ν_{CM} is the x-axis centre-of-mass mode frequency (which is the highest one, if x axis trapping frequency ω_x is higher than ω_y) and $\nu_{\text{CM}} \gg \Delta \gg \delta$. The corresponding detuned red and blue sideband Hamiltonians, after applying the vibrational RWA, read

$$
H^{\text{d/rsb}} = \sum_{i=1}^{N} \sum_{m=1}^{2N} i\frac{\hbar}{2}\Omega_i \eta_{i,m} \sigma_i^+ a_m e^{i(\Delta_m - \delta)t} e^{i\phi_r} + \text{H.c.}
\tag{3.35}
$$

$$H^{\text{d/bsb}} = \sum_{i=1}^{N} \sum_{m=1}^{2N} i\frac{\hbar}{2}\Omega_i \eta_{i,m}\sigma_i^+ a_m^\dagger e^{-i(\Delta_m+\delta)t}e^{i\phi_b} + \text{H.c}, \tag{3.36}$$

where $\Delta_m = \Delta + \nu_{\text{CM}} - \nu_m$. Redefining the phases as $\phi_M = \frac{\phi_r-\phi_b}{2}$ and $\phi_S = \frac{\phi_r+\phi_b+\pi}{2}$, the sum of both Hamiltonians can be written in the following way

$$H_{BIC} = \sum_{i=1}^{N} \sum_{m=1}^{2N} \frac{\hbar}{2}\Omega_i \eta_{i,m}(\sigma_i^+ e^{-i(\delta t-\phi_S)} + \sigma_i^- e^{i(\delta t-\phi_S)})(a_m e^{i(\Delta_m t+\phi_M)} + a_m^\dagger e^{-i(\Delta_m t+\phi_M)}). \tag{3.37}$$

For the sake of simplicity, to derive the spin-spin effective Hamiltonians, we will consider the presence of a single mode. The introduction of more modes only affects the resultant spin-spin coupling strength J_{ij}. Setting ϕ_r and ϕ_b to $\phi_r = \phi_b = -\pi/2$, so that $\phi_M = \phi_S = 0$, taking the same Rabi frequency for every ion ($\Omega_i = \Omega$) and defining $\sigma^\pm = \sum_i \sigma_i^\pm$, the Hamiltonian in Eq. (3.37) considering only the centre of mass CM mode (where $\eta_{i,\text{CM}} = \eta$ for every ion) is written

$$H_{BIC} = \eta\frac{\hbar\Omega}{2}(\sigma^+ e^{-i\delta t} + \sigma^- e^{i\delta t})(ae^{i\Delta t} + a^\dagger e^{-i\Delta t}). \tag{3.38}$$

As we have done in section 3.1.1, we will write the time evolution of the Hamiltonian in Eq. (3.38) using the first two terms of the Magnus expansion

$$U(t) = e^{\Omega_1(t)+\Omega_2(t)+\cdots} \tag{3.39}$$

The integral in the first term $\Omega_1(t)$ contains four terms that oscillate with frequencies of the order of Δ. Since $\Delta \gg J$, J being the value for the spin-spin coupling strength ($J = \frac{\Omega^2\eta^2}{4\Delta}$), we can neglect the oscillating terms and ingnore the first order, using the same arguments that we used in section 3.1.1. It is said that those contributions are *adiabatically eliminated*, however, the approximation holds on the equal footing as the RWA.

For the second order term $\Omega_2(t)$ we need to calculate the following commutator

$$[H(t_1), H(t_2)] = (\frac{\hbar\Omega\eta}{2})^2[(\sigma^+ e^{-i\delta t_1} + \sigma^- e^{i\delta t_1})(ae^{i\Delta t_1} + a^\dagger e^{-i\Delta t_1}),$$
$$(\sigma^+ e^{-i\delta t_2} + \sigma^- e^{i\delta t_2})(ae^{i\Delta t_2} + a^\dagger e^{-i\Delta t_2})], \tag{3.40}$$

$$[H(t_1), H(t_2)] = (\frac{\hbar\Omega\eta}{2})^2\{(ae^{i\Delta t_1} + a^\dagger e^{-i\Delta t_1})(ae^{i\Delta t_2} + a^\dagger e^{-i\Delta t_2})(e^{-i\delta(t_1-t_2)} - e^{i\delta(t_1-t_2)})\sigma^z$$
$$+ \sum_{i,j}(\sigma_i^+ e^{-i\delta t_1} + \sigma_i^- e^{i\delta t_1})(\sigma_j^+ e^{-i\delta t_2} + \sigma_j^- e^{i\delta t_2})(e^{i\Delta(t_1-t_2)} - e^{-i\Delta(t_1-t_2)})\}. \tag{3.41}$$

If we follow the recipe described in section 3.1.1, and if we calculate the first integral from $\Omega_2(t)$, and then adiabatically eliminate the terms that oscillate with frequencies of the order of Δ, it can be proven, after some calculations, that $\Omega_2(t)$ can be simplified to

$$\Omega_2(t) = -i\frac{\Omega^2\eta^2}{8}\int_0^t dt_1\{(2a^\dagger a + 1)\frac{\delta}{\Delta^2}\sigma^z + \sum_{i,j}\frac{1}{\Delta}(\sigma_i^+\sigma_j^+ e^{-2i\delta t_1} + \sigma_i^+\sigma_j^- + \text{H.c})\}, \quad (3.42)$$

which gives the effective Hamiltonian

$$H_{\text{eff}} = \frac{\hbar}{2}J\{(2a^\dagger a + 1)\frac{\delta}{\Delta}\sigma^z + \sum_{i,j}(\sigma_i^+\sigma_j^+ e^{-2i\delta t} + \sigma_i^+\sigma_j^- + \sigma_i^-\sigma_j^+ + \sigma_i^-\sigma_j^- e^{2i\delta t})\}, \quad (3.43)$$

where N is the number operator. From this expression we can see that there are terms depending on the number of phonons as soon as $\delta \neq 0$. The asymmetrical detuning leads to slightly different coupling strengths in the red and blue sidebands, from where the phonon dependency arises. Depending on δ, we can identify three regimes in H_{eff}.

Regime 1 In the case where $\delta \ll J$, we can simply let $\delta \to 0$, and the effective Hamiltonian reads

$$H_{\text{eff}} = \frac{\hbar}{2}J\sum_{i,j}(\sigma_i^+\sigma_j^+ + \sigma_i^+\sigma_j^- + \sigma_i^-\sigma_j^+ + \sigma_i^-\sigma_j^-) = \frac{\hbar}{2}J\sum_{i,j}\sigma_i^x\sigma_j^x. \quad (3.44)$$

If we consider all the radial modes, the only thing that changes is that the coupling strength is now given by a more complicated expression

$$H_{xx} = \frac{\hbar}{2}\sum_{i,j}J_{ij}\sigma_i^x\sigma_j^x = \hbar\sum_{i<j}J_{ij}\sigma_i^x\sigma_j^x, \quad (3.45)$$

where

$$J_{ij} = \frac{\Omega_i\Omega_j}{2}\sum_{m=1}^{2N}\frac{\eta_{i,m}\eta_{j,m}}{\Delta_m}. \quad (3.46)$$

If we set the initial laser phases to $\phi_r = \phi_b = 0$, we generate the H_{yy} Hamiltonian

$$H_{yy} = \hbar\sum_{i<j}J_{ij}\sigma_i^y\sigma_j^y. \quad (3.47)$$

In this regime, the effective Hamiltonian does not depend on the modes so it is not necessary to care about their heating, up to a certain extent.

Regime 2 If we assume that $\delta \gg J$, the phases of the double spin-flip terms $\sigma_i^+\sigma_j^+$ and $\sigma_i^-\sigma_j^-$ in Eq. (3.43) are rotating fast and thus can be eliminated. The Hamiltonian that results is an H_{xy} with a small phonon-dependent transverse field, which considering all modes reads

$$H_{\text{eff}} = \hbar\sum_{i<j}J_{ij}(\sigma_i^+\sigma_j^- + \sigma_i^-\sigma_j^+) + \hbar\sum_{i=1}^N\hat{\mathcal{B}}_i\sigma_i^z, \quad (3.48)$$

where

$$\hat{\mathcal{B}}_i = \delta\Omega_i^2 \sum_m \Big(\frac{\eta_{i,m}}{\Delta_m}\Big)^2 \Big(N_m + \frac{1}{2}\Big). \tag{3.49}$$

As we can see, we have a transerve field that depends on the phonon number of each mode N_m. If we cool all the modes to the ground state, typically $\sum_i \langle \mathcal{B}_i \rangle$ is one order of magnitude smaller than J. In this case, we can assume that our effective Hamiltonian is

$$H_{xy} = \hbar \sum_{i<j} J_{ij}(\sigma_i^+\sigma_j^- + \sigma_i^-\sigma_j^+) = \frac{\hbar}{2}\sum_{i<j} J_{ij}(\sigma_i^x\sigma_j^x + \sigma_i^y\sigma_j^y). \tag{3.50}$$

However, if the modes are not properly cooled down, this transverse field imprints a differential AC-Stark shift onto the ions, since all modes except the CM mode have a non-uniform distribution of the mode-vector amplitudes $\mathcal{M}_{i,m}$ across the string. To prevent this problem, we need to cool down the modes well below a single phonon.
Nevertheless, the heating of the modes during the time-evolution cannot be avoided, so even if they are perfectly cooled to the ground state, they would eventually heat up. Fortunately, the normal mode with the highest heating rate happens to be the CM mode, which is the only one that has a uniform mode-vector and therefore wil cause all ions to get the same AC-stark shift.

There may be cases, hovever, where we need to have an H_{xy} Hamiltonian along with a strong transverse field. We can easily get this by writing $H_{\mathrm{eff}} = H_\delta + (H_{\mathrm{eff}} - H_\delta)$, and changing into an interaction picture with respect to $H_\delta = -\hbar\frac{\delta}{2}\sigma^z$. Note that H_{xy} commutes with this Hamiltonian so the frame change is straightforward

$$H'_{\mathrm{eff}} = e^{iH_\delta t/\hbar}(H_{\mathrm{eff}} - H_\delta)e^{-iH_\delta t/\hbar} = \hbar J_{ij}\sum_{i<j}(\sigma_i^+\sigma_j^- + \sigma_i^-\sigma_j^+) + \hbar B\sigma^z. \tag{3.51}$$

where the effective transverse field is $B = -\delta/2$.

Regime 3 This regime is the intermediate case where $\Delta \gg \delta \approx J$. In this case, the rotating terms must not be eliminated but we do not have to care about the $\hat{\mathcal{B}}$ field. Taking once again all the modes into account the Hamiltonian reads

$$H_{\mathrm{eff}} = \hbar \sum_{i<j} J_{ij}(\sigma_i^+\sigma_j^+ e^{-2i\delta t} + \sigma_i^+\sigma_j^- + \sigma_i^-\sigma_j^+ + \sigma_i^-\sigma_j^- e^{2i\delta t}). \tag{3.52}$$

Following the same procedure as in the H_{xy} region, we change to a picture where the Hamiltonian is time independent. In this picture, the effective Hamiltonian describes an Ising model with a transverse field $B = -\delta/2$

$$H_{\mathrm{Ising}} = H'_{\mathrm{eff}} = \hbar \sum_{i<j} J_{ij}\sigma_i^x\sigma_j^x + \hbar B\sigma^z. \tag{3.53}$$

Chapter 4

Digital-Analog Quantum Simulation of Spin Models in Ion Traps

In this chapter, we propose the simulation of the Heisenberg spin-1/2 chain using a digital-analog approach. First, we will introduce the novel concept of digital-analog quantum simulations. In section 4.2, we will propose different approaches for the digitization of Heisenberg dynamics and compare them, focusing on their digital error. In section 4.3, we will compare the digital-analog protocol with a purely digital one, considering gate fidelities and digital errors. The last two sections are devoted to the implementation of these techniques in trapped ions. This chapter represents the heart of this thesis, containing a novel and original proposal for the simulation of the Heisenberg model in trapped ions.

Proposals for the analog trapped-ion simulation of the Heisenberg model exist in the literature. In one of these proposals, the authors suggest to use the vibrational modes in all directions to generate an effective Heisenberg spin-1/2 interaction [13, 44]. This proposal, however, shows problems for a real implementation because, among other things, the modes in the longitudinal axis are highly susceptible of heating. In our proposal, only the modes in the radial axes take part on the generation of the effective spin-spin interactions. The other proposal is about simulating the Haldane phase using optical fields in trapped ions. For that, they have to implement a $s = 1$ Heisenberg model and they achieve this by the use of several lasers [45].

4.1   Digital-Analog approach

In 1996, Seth Lloyd showed that a controllable many-body quantum system can be programmed to simulate any local quantum system efficiently [19]. We call these envisioned quantum devices universal digital quantum simulators. Digital quantum simulations can perform a universal set of quantum operations (gates) with which we could, in

principle, design a protocol or algorithm to carry out the simulation. However, taking into account the current technological limitations, the construction of a universal digital quantum simulator is a hard challenge.

In the pursue of a universal quantum simulator, like the one conjectured by Feynman and proposed by Lloyd, we try to construct quantum devices that are able to implement universal gates, which arise from dynamics that are unnatural to the devices themselves. However, quantum platforms are ruled by much more complex evolutions from which we could profit for quantum simulation, since these arise more spontaneously. These evolutions are typically considered as analog quantum simulations of certain physical model, something that we can call a purpose specific quantum simulator, in contrast to the universal quantum simulator. Some examples of this have already seen the light [16, 25, 39, 40]. Purpose specific digital quantum simulations have been also implemented in platforms that do not still constitute a universal quantum computer, but can perform a reduced set of gates, capable of digitally simulating a specific model of interest.

The core of this thesis is to propose a merge between this two approaches, namely the digital and the analog ones, to go beyond the capabilities of both of them, in the absence of a universal quantum simulator. Digital-analog quantum simulators are not so much based in universal quantum gates, but in analog blocks and digital steps. An analog block is by itself an analog quantum simulation of a non-trivial quantum model, and in this sense, it is particular of a specific quantum platform. In a digital-analog protocol, we treat these analog blocks as gates, with the intention to simulate quantum systems that are more complicated than the ones that the analog block simulates. Along with them, the digital-analog approach makes use of digital steps, such as global qubit rotations. In this sense, digital-analog quantum simulators combine digital steps with analog blocks.

Digital-analog quantum simulators are not intended to specifically simulate local quantum system, as universal digital simulators. But they can allow to carry out simulations of some complex systems that are impossible with current analog or digital quantum simulators.

During the whole chapter, we will differentiate two kinds of protocols. We will call purely or fully digital protocols to those that are composed by one and two-qubit gates and hence, are valid protocols for any universal quantum simulator. And we will call digital-analog protocols to the ones that use analog blocks along with digital steps consisting in one- and two-qubit gates.

4.2   Digitization of the Heisenberg model

In this section, we will discuss the various options to digitize the evolution of the Heisenberg Hamiltonian, using digital-analog techniques. As analog blocks, we will use different effective Hamiltonians that can be implemented in trapped ions, which we have introduced already in chapter 3.2.

The most general antiferromagnetic Heisenberg Hamiltonian for a spin-1/2 chain can

be expressed as $(\hbar = 1)$

$$H_{\text{HB}} = \sum_{i<j} J_{ij}(\sigma_i^x \sigma_j^x + \sigma_i^y \sigma_j^y + \sigma_i^z \sigma_j^z) \tag{4.1}$$

with $J_{i,j}$ ranging from nearest-neighbors to long-range couplings. Although a fully digital approach would suggest to split the Hamiltonian into single two-body interactions as $J_{ij}\sigma_i^x \sigma_j^x$, we will split the Hamiltonian into two or three parts taking advantage of the natural effective Hamiltonians that we find in trapped ions. Three possible ways of splitting the Hamiltonian are the following

$$\text{partition 1} \quad H_{\text{HB}} \; = \; H_{xx} + H_{yy} + H_{zz} \tag{4.2}$$

$$\text{partition 2} \quad H_{\text{HB}} \; = \; \frac{1}{2}(H_{xy} + H_{yz} + H_{zx}) \tag{4.3}$$

$$\text{partition 3} \quad H_{\text{HB}} \; = \; H_{xy} + H_{zz}. \tag{4.4}$$

We will assume that the H_{xx} and H_{xy} Hamiltonians, introduced in chapter 3, are efficiently implementable in trapped ions. In order to obtain the unitary evolution produced by, H_{zz}, H_{yz} and H_{zx}, we can use global qubit rotations $R_{x(y)}(\pi/4)$, which can be implemented driving the ions into resonance with the carrier transition. The following transformations will provide us with the desired interaction Hamiltonians in the following way $(R_{x(y)} \equiv R_{x(y)}(\pi/4))$,

$$H_{zz} \; = \; R_y H_{xx} R_y^\dagger \tag{4.5}$$

$$H_{yz} \; = \; R_y H_{xy} R_y^\dagger \tag{4.6}$$

$$H_{zx} \; = \; R_x H_{xy} R_x^\dagger. \tag{4.7}$$

According to partition 1, the Heisenberg Hamiltonian could be implemented, following Trotter techniques introduced in chapter 1, iterating l times the following algorithm:

Step1. The qubits interact for a time t/l according to the H_{xx} Hamiltonian.
Step2. Application of a global rotation $R_y^\dagger(\pi/4)$ to all qubits.
Step3. The qubits interact for a time t/l according to the H_{xx} Hamiltonian.
Step4. Application of a global rotation $R_y(\pi/4)$ to all qubits.
Step5. The qubits interact for a time t/l according to the H_{yy} Hamiltonian.

In Fig. 4.1, protocols P1, P2 and P3 are shown, based in Eqs. (4.2), (4.3) and (4.4), respectively.

In general, the larger the time we want to simulate, the larger the number of Trotter steps that are needed to maintain the approximation, due to the non-commutativity of the different Hamiltonians. Additionally, notice that doing more Trotter steps hardly affects the experimental simulation time. This is because in trapped ions the global rotations are three orders of magnitude faster than the analog gates. Moreover, we can symmetrize the Hamiltonians to avoid the second-order error of the Trotter expansion,
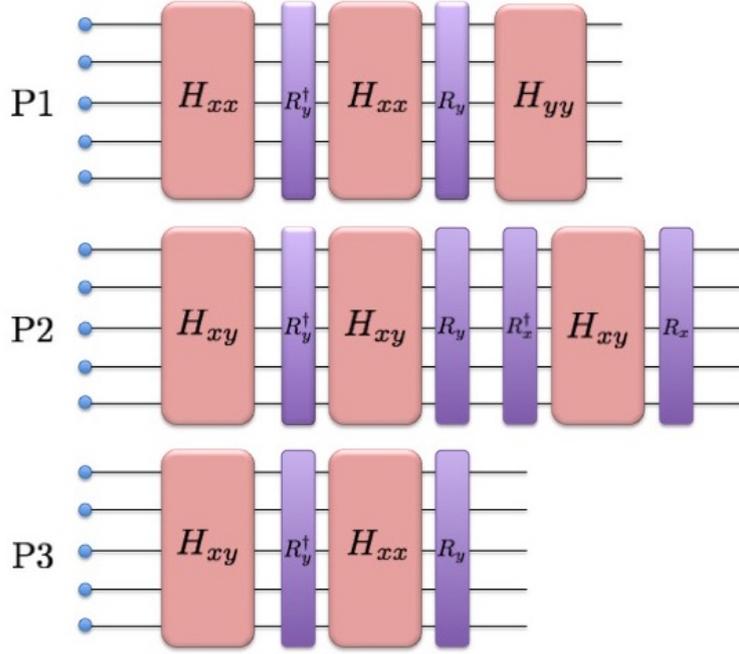
Figure 4.1: Digital-analog protocols for a Trotter step according to partitions 1,2 and 3.

but the prize that we have to pay is that we need to introduce more gates in each Trotter step. However, sometimes it is worthwhile. For example, for the third partition, the Trotterization of the evolution operator will correspond to

$$e^{-iH_{\mathrm{HB}}t} \simeq (e^{-iH_{xy}t/l}e^{-iH_{zz}t/l})^l, \tag{4.8}$$

while in the simetrized case

$$e^{-iH_{\mathrm{HB}}t} \simeq (e^{-iH_{xy}t/2l}e^{-iH_{zz}t/l}e^{-iH_{xy}t/2l})^l. \tag{4.9}$$

Note that we have introduced one more gate in each Trotter step. But if we look carefully, we can realize that the last gate of each Trotter step and the first gate of the following step are identical. So instead of doing twice the same gate, we can simply do a single gate for a double time. Finally, the simetrized protocol needs only one more gate than the non-simetrized one. The whole protocol, that we will call P4, is shown in Fig. 4.2

The purpose of the protocols is to produce a dynamics as close as possible to the dynamics of the Heisenberg model, using the fewest number of Trotter steps. However, before we start comparing the different protocols we should try to gather some intuition about how the Trotter error is going to depend not in the used protocol, but in general features of the simulated model.
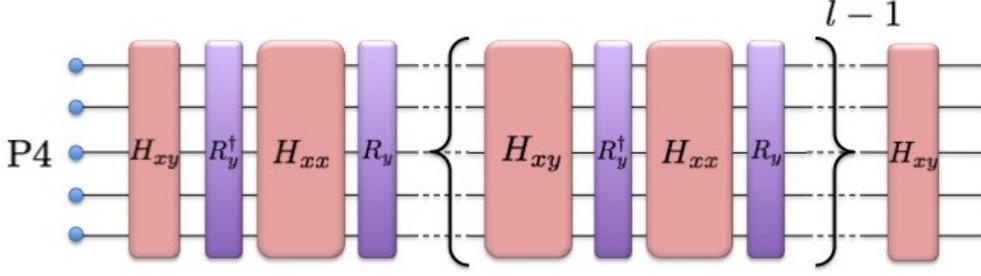
Figure 4.2: Whole simetrized digital-analog protocol for l Trotter steps. Because of the few number of gates in P3, the simetrization of the protocol is accomplished by introducing only one more analog block.

In general, the Trotter approximation is a compromise between the time that we want to simulate and the number of Trotter steps. At very short times, few numbers of Trotter steps are needed to maintain the approximation. However, the maximum Trotter error that we can have has this form,

$$O_{max}(t^2) = \sum_{k=2}^{\infty} \|H\|_{sup}^k \frac{t^k}{k!l^{k-1}} = \|H\|_{sup}^2 \frac{t^2}{2l} + \|H\|_{sup}^3 \frac{t^3}{6l^2} + \dots \qquad (4.10)$$

where t is the simulation time and l the number of Trotter steps. $\|H\|_{sup}$ is the energy of the most excited state of our Hamiltonian. In our case, we have to deal with the Heisenberg Hamiltonian, where this maximum energy will increase with the number of spins that we consider and the range of interaction J_{ij}. On any antiferromagnetic Hamiltonian, states that have all spins aligned along the same direction, i.e. $|\uparrow\uparrow \cdots \uparrow\rangle$ and $|\downarrow\downarrow \cdots \downarrow\rangle$, happen to be part of the most energetic ones. The energy for these states given any Heisenberg Hamiltonian is

$$E_{max} = \|H\|_{sup} = \frac{1}{4} \sum_{i<j} J_{ij}. \qquad (4.11)$$

For the NN model, this gives an upper bound of $(N_s - 1)J$, whereas for the LMG model gives $N_s(N_s - 1)J/2$. The energy raises while we increase the number of interactions in our system. Taking the maximum possible second order error, for 8 spins, the LMG would have a second order digital error 16 times larger than the NN model.

Of course, all the arguments given above are based on the upper bound terms, but the Trotter error depends more particularly on the decomposition of the Hamiltonian. So in order to evaluate the accuracy of our different protocols we introduce the fidelity between two states ψ_1 and ψ_2 as $F = |\langle\psi_1|\psi_2\rangle|^2$, which will give us a measure of the distance between the state that our evolution is producing and the one that an ideal Heisenberg Hamiltonian would produce.
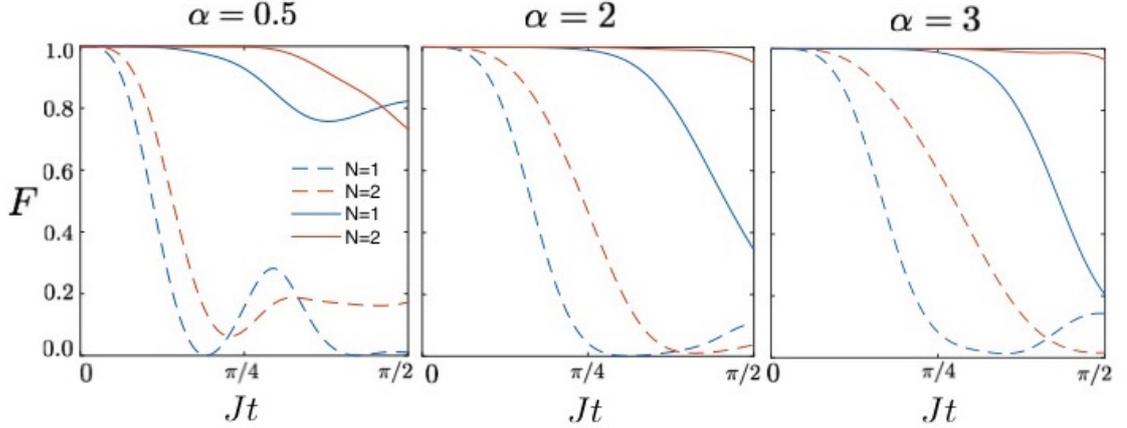
Figure 4.3: Fidelities obtained with initial state $|\downarrow\downarrow\downarrow\uparrow\downarrow\downarrow\downarrow\rangle$ for 7 spins. Dashed lines follow protocol P1 while solid lines follow protocol P4. Blue and orange lines correspond to one and two Trotter steps respectively.

In Fig 4.3, we have plotted the fidelities obtained with an initial state $|\downarrow\downarrow\downarrow\uparrow\downarrow\downarrow\downarrow\rangle$ for protocol 1 (dashed lines) and protocol 4 (solid lines), considering one (blue) and two (orange) Trotter steps for 7 spins. We have evaluated the protocols for three different regimes of the Heisenberg model where we have taken J_{ij} to be of the form $J/|i-j|^{\alpha}$ in a way which the different regimes are charactized by α. $\alpha = 0$ and $\alpha = \infty$ are the LMG and NN models respectively, however, $\alpha = 3$ can also be approximated as the NN model.

If we look at Fig. 4.3, the first thing we notice is that protocol P4 (solid lines) is the one that gives the best results. The same is true if instead of P1, we compare to P2 or P3. On the other hand, from the arguments given before, we should expect the digital error to increase while we go from a short-range ($\alpha = 3$) to a long-range ($\alpha = 0.5$) Hamiltonian. However, we can see that P4 does not follow this behaviour, it even improves when in the long-range case. This does not mean that the arguments above are worthless, actually, if we look at the difference between a single or a double Trotter step, we find that to do a second Trotter step is more beneficial in the short-range case than in the long-range one. This happens in both of the protocols, and it is a sign that the Trotter error gets more significant while we shorten the interaction range.

The explanation of why protocol 4 gets better when α goes to zero is found in the LMG model, where the protocol follows without error the Heisenberg dynamics. Protocol 4 is composed only by H_{xy} and H_{zz} analog blocks, and in the LMG model, these two Hamiltonians commute.
Taking into account that the simulation of Hamiltonians such as the long-range Heisenberg Hamiltonian, is especially difficult with fully digital approaches, we conclude that P4 is the most competitive digital-analog protocol among the ones that we studied, and thus the first candidate for a real implementation in trapped ions.
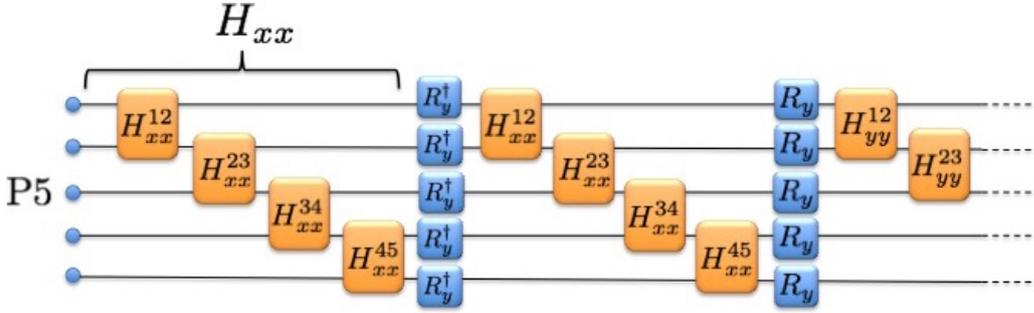
Figure 4.4: Purely digital Trotter step based in Eq. (4.2) for simulating the NN Heisenberg chain.

4.3   Digital-analog versus purely digital

For the quantum simulation of a many-body Hamiltonian, the main difference between a digital-analog and a purely digital protocol is that the analog gate provides us many-body Hamiltonians in a single gate while the fully digital way requires to perform at least one gate for every two-body interaction (characterized by J_{ij}, in our case) present in our model. In this sense, a purely digital protocol will of course need much more gates, but this is not necessarily bad for the digital error.

Protocol P5, shown in Fig. 4.4, is a purely digital protocol for the simulation of the NN Heisenberg chain. As a matter of fact, we would say that this purely digital protocol is based on P1, because it has the same structure except for the fact that the analog blocks are now formed by multiple two-qubit gates, and instead of global rotations, single-qubit rotations are performed. Additionally, in fully digital cases, we need to design a protocol for each model. For example, to simulate the LMG model, we need to design a different protocol, which is going to follow the same structure of P1, but in this case, in substitution of the analog block, we have to follow the scheme in Fig 4.6. We will call this protocol P6. Both of these protocols produce the same Trotter error as P1 and this is because all the two-qubit gates that substitute the analog block commute with each other. However, this does not hold for the other cases.

If we construct a fully digital protocol based on P2, the digital error of this protocol will be larger than the error of its digital-analog counterpart. A similar thing happens with a protocol based on P3 or P4. In Fig. 4.5, we have plotted the fidelities obtained using the digital-analog protocol P3, and the fully digital protocol based in it, that uses H_{xy} two-qubit gates. Notice that the fully digital protocol shows more digital error. In general, using H_{xy} two-qubit gates in a fully digital protocol to simulate many body Hamiltonians is not convenient, because $[H_{xy}^{ij}, H_{xy}^{ij'}] \neq 0$, if $j' \neq j$. That is why we assume only the use of H_{xx} two-qubit gates for purely digital protocols. We conclude, that in the best of the cases, the fully digital protocol shows the same digital error as the digital-analog protocol. In this sense, it does not look particularly meaningful to
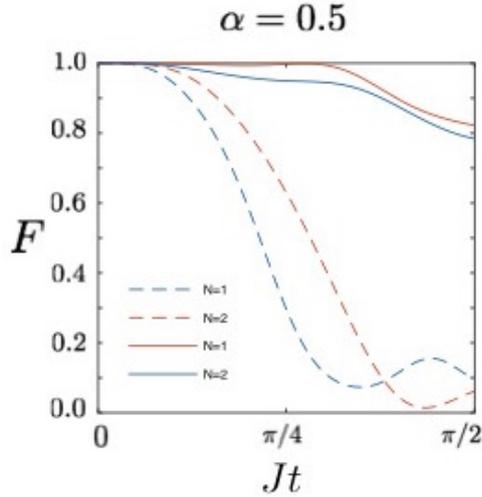
Figure 4.5: Fidelities obtained with initial state $|\downarrow\downarrow\uparrow\downarrow\downarrow\rangle$ for 5 spins. Solid lines follow protocol P3 while dashed lines follow a fully digital protocol based in P3. Blue and orange lines correspond to one and two Trotter steps respectively.

compare the digital error caused by a fully digital protocol and a digital-analog one.

Apart from the Trotter error, any realistic digital simulation has to deal with another source of error coming from each gate, experimental error. Gate fidelities quantify the distance between the produced state and the one we wanted to produce after applying a gate. As we said before, a fully digital protocol will certainly need a larger number of gates. Actually, the protocol shown in Fig. 4.4 needs $3(N_s - 1)$ two-qubit gates and $2N_s$ single-qubit rotations on each Trotter step, for N_s spins. It gets harder for the LMG model, where we need to perform $3N_s(N_s - 1)/2$ gates and $2N_s$ rotations on each Trotter step.

However, taking into account that these gates are only one- and two-qubit gates, it is fair to consider that these gates will have higher gate fidelities than the analog blocks. In this sense, a purely digital proposal would need to compensate the large number of gates needed with better gate fidelities. One of the main tasks of this chapter is to discuss about the scalability of the digital-analog and the purely digital proposals considering realistic gate fidelities.

We will assume a two-qubit gate fidelity of $F_D = 99, 4\%$ [12], and in the case of the analog blocks we will consider three possible values, namely $F_{DA} = 80\%$, 90% and 95%. To avoid an excessive number of variables we will take the single-qubit gates and the global rotations as perfect [11]. Now that we have introduced the concept of gate fidelity, the simulation will not necessarily improve when we increase the number of Trotter steps N. This is because doing more steps means increasing the error coming from the gates. In this sense, we will have to find an optimal number of Trotter steps depending on the gate fidelities and the simulated time. Furthermore, this number will also depend on the simulated model or the protocol used to perform the simulation.
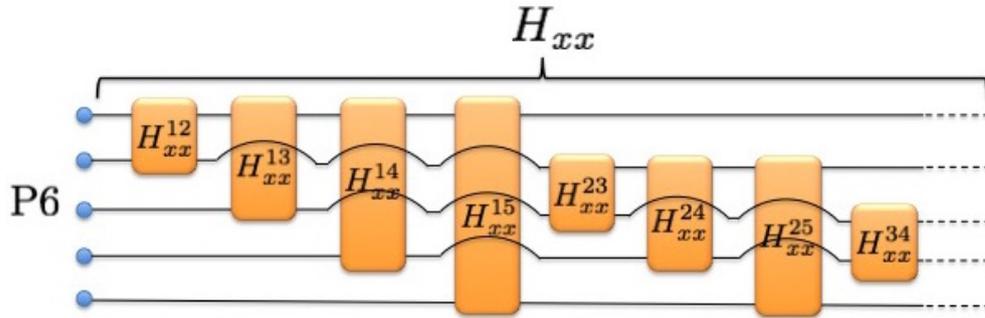
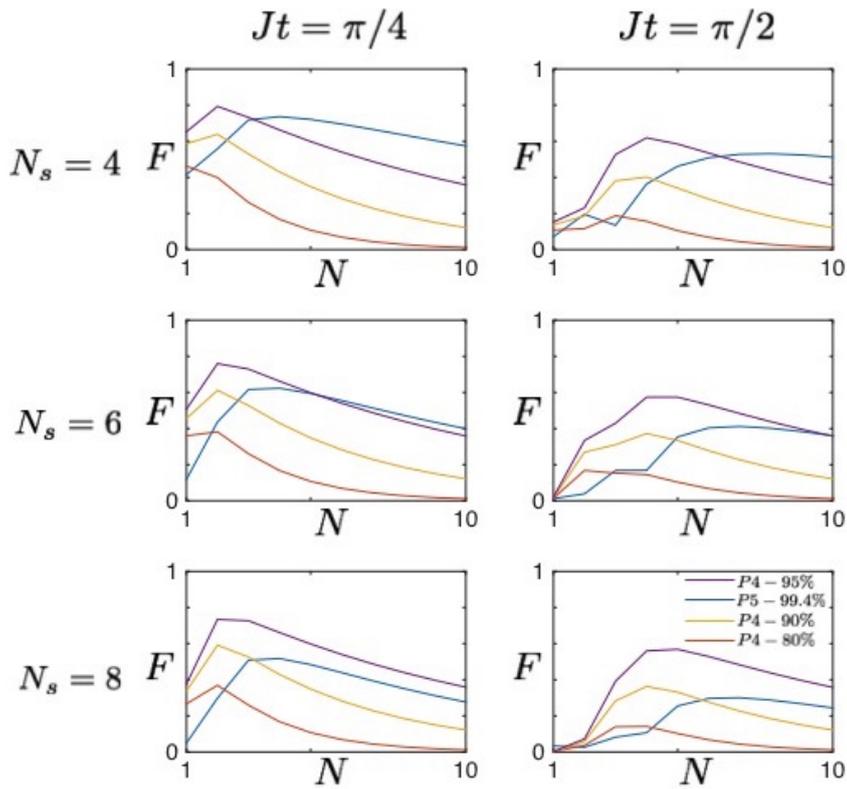Figure 4.6: Scheme for the generation of the H_{xx} Hamiltonian in the LMG model, in the case of 5 spins.

Figure 4.7: Fidelities obtained in the simulation of the NN model for different times and number of spins N_s, using P5 (blue) and P4 (orange, yellow, purple). Because of the gate errors, the simulation does not necessarily improve increasing the number of Trotter steps N.
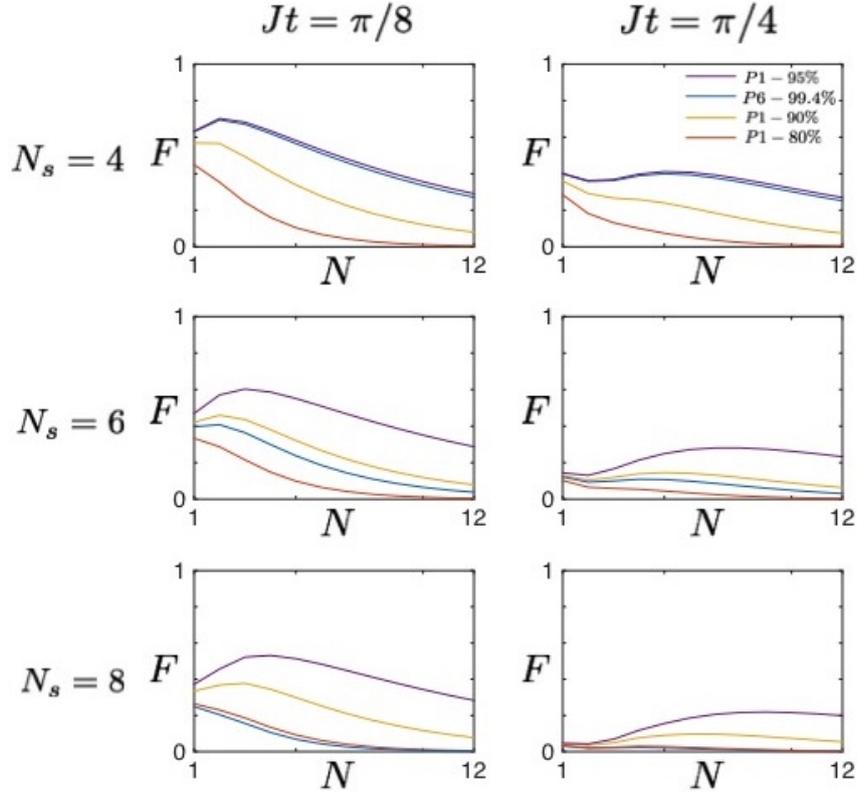
Figure 4.8: Fidelities obtained in the simulation of the LMG model for different times and number of spins N_s, using P6 (blue) and P1 (orange, yellow, purple).

In Fig. 4.7 we compare fidelities obtained with initial states $|\uparrow\downarrow\uparrow\downarrow\rangle$, $|\uparrow\downarrow\uparrow\downarrow\uparrow\downarrow\rangle$ and $|\uparrow\downarrow\uparrow\downarrow\uparrow\downarrow\rangle$ as a function of the number of Trotter steps, in simulating the NN model. Blue lines follow the fully digital protocol P5 while the others follow P4. We want to emphasize how the fidelities obtained with P5 decay while we increase the number of spins N_s. With 4 spins P5 uses 9 two-qubit gates per step and we can reach more or less the same fidelities using both protocols. However, with 8 spins, we begin to see the benefit of using a digital-analog protocol. With $N_s = 8$, P5 already requires 21 two-qubit gates per step. Fig. 4.7 includes data for the simulation of the NN model, which is the less harmful one for the fully digital approach. If we look into the simulation of a long-range model such as the LMG model, the fidelities will decay more dramatically with the number of spins.

In Fig. 4.8, we have plotted the fidelities obtained for the simulation of the LMG model. We have used P1 instead of P4 -because the last one is specially good in the simulation of LMG model- in a way that the Trotter error of the fully digital and the digital-analog protocols are identical. Notice that we have lowered the simulated time, because for longer times the digital error gets very large. For the case of 4 spins, P6

obtains fidelities equivalent to P1 with the best gate fidelity. This also happened for the NN model. Nevertheless, for $N_s = 6$ the fidelities of the fully digital protocol clearly fall down. For $N = 8$ the protocol is comparable with the digital-analog protocol with worst gate fidelity.

All in all, we have show that fully digital protocols typically involve a higher Trotter error than the digital-analog ones. Additionally, we have seen that, even if F_D is one order of magnitude better than F_{DA}, if we go beyond $N_s = 4$ spins, the purely digital protocol is worse than our best digital-analog protocol. These facts make the presented digital-analog technique a suitable alternative to purely digital protocols.

4.4   Numerical simulations

On the previous section, we have compared digital-analog and purely digital approaches for simulating the Heisenberg model. The discussion was not framed in any specific quantum platform, but our proposal is based on the H_{xx} and H_{xy} analog blocks that we find in trapped ions. Consequently, it is our duty to specify which are the inconveniences or errors that a current trapped-ion platform would show while carrying out our proposal. In this section, we will make numerical simulations of the whole digital-analog protocol using trapped-ion Hamiltonians. In section 3.2.1, we explained how the H_{xx} and H_{xy} analog blocks are generated, where we made several approximations. Especially, we care about the adiabatic eliminations, which we identify as the main source of error for the analog-blocks. We have made numerical simulations of the spin-spin effective Hamiltonian H_{xx} starting from the typical first-principles trapped-ion Hamiltonian [41]

$$H_{\text{BIC}} = \sum_{i=1}^{N_s} \sum_{m=1}^{2N_s} \frac{\hbar}{2} \Omega_i \eta_{i,m} \sigma_i^x (a_m e^{i\Delta_m t} + a_m^\dagger e^{-i\Delta_m t}). \tag{4.12}$$

with the presence of all the $2N_s$ radial modes. If we simulate a Hilbert space of $N_{\text{trun}} = 3$ for every normal mode, we are only able to simulate two ions with our computational resources. In this sense, we have to think of some technique to carry out the simulation for many ions. Note that the Hamiltonian (4.12) can be written in a time-independent way if we go to an interaction picture characterised by $H_0 = \hbar \sum_m \Delta_m a_m^\dagger a_m$. In this picture, the Hamiltonian is written in the following way

$$H = -\hbar \sum_{m=1}^{2N_s} \Delta_m a_m^\dagger a_m + \sum_{i=1}^{N_s} \sum_{m=1}^{2N_s} \frac{\hbar}{2} \Omega_i \eta_{i,m} \sigma_i^x (a_m + a_m^\dagger). \tag{4.13}$$

Now, we may note that the Hamiltonian can be seen as a sum of $2N_s$ Hamiltonians, one for each radial mode

$$H = \sum_{m=1}^{2N_s} H_m \tag{4.14}$$

where

$$H_m = -\hbar \Delta_m a_m^\dagger a_m + \sum_{i=1}^{N_s} \frac{\hbar}{2} \Omega_i \eta_{i,m} \sigma_i^x (a_m + a_m^\dagger). \tag{4.15}$$

Each of the H_m Hamiltonians commute with all the others. This allows us to see the evolution in $2N_s$ steps, in other words, to see the contribution of each mode separately, in a way that each step has to take into account only the contribution of a single mode. According to the approximations explained in Section 3.2.1, the whole evolution should effectively behave as a spin-spin coupling, so we are going to look to the spin part of the final state ignoring the motional states. Thus, we are going to trace out the motional part. Instead of tracing out all the $2N_s$ motional subspaces, whenever we have the final state, we are going to trace the m-th mode subspace right after $U_m = e^{-iH_0^m} e^{-iH_m t}$ acts in the corresponding state. With a little bit more mathematical rigour, our final state will be given by the following density matrix

$$\rho(t) = \mathrm{Tr}_{2N_s} \cdots \mathrm{Tr}_1 (U_{2N_s} \cdots U_1 \rho_0 U_1^\dagger \cdots U_{2N_s}^\dagger) \tag{4.16}$$

which can be proven to be equivalent to

$$\rho(t) = \mathrm{Tr}_{2N_s} (U_{2N_s} \cdots \mathrm{Tr}_1 (U_1 \rho_0 U_1^\dagger) \cdots U_{2N_s}^\dagger). \tag{4.17}$$

Thanks to that property, we can simulate the contribution of the radial modes by doing $2N$ calculations in a Hilbert space of $N_{\mathrm{trun}} \otimes 2_s^N$ dimensions, instead of doing a single calculation in a space of $N_{\mathrm{trun}}^{2N_s} \otimes 2_s^N$.

Using this property we have been able to simulate in our computers the H_{xx} analog gate for more than 7 ions. This method, however, cannot be used to simulate the H_{xy} interaction. This last interaction is obtained effectively from Hamiltonian

$$H_{\mathrm{LD}} = \sum_{i=1}^{N_s} \sum_{m=1}^{2N_s} \frac{\hbar}{2} \Omega_i \eta_{i,m} (\sigma_i^+ e^{-i\delta t} + \sigma^- e^{i\delta t})(a_m e^{i\Delta_m t} + a_m^\dagger e^{-i\Delta_m t}), \tag{4.18}$$

in a region where δ is larger than the effective spin-spin coupling strength. The time independent version of this Hamiltonian is obtained by going to an interaction picture characterised by $H_0 = \hbar\delta/2 \sum_i \sigma_i^z + \hbar \sum_m \Delta_m a_m^\dagger a_m$ and where the interaction Hamiltonian is

$$H = -\hbar\frac{\delta}{2} \sum_i^{N_s} \sigma_i^z - \hbar \sum_{m=1}^{2N_s} \Delta_m a_m^\dagger a_m + \sum_{i=1}^{N_s} \sum_{m=1}^{2N_s} \frac{\hbar}{2} \Omega_i \eta_{i,m} \sigma_i^x (a_m + a_m^\dagger). \tag{4.19}$$

Note that this Hamiltonian cannot be rewritten as a sum of H_m commuting Hamiltonians anymore. This makes impossible the simulation of the H_{xy} interaction using the method presented above. Nevertheless, we can simulate at least the H_{xx} analog gate, which is enough if we take the digital-analog protocol P1.

The simulation requires the control of N_s spins, but in trapped ions we have to deal with the motional states also. Nevertheless, if we are interested in considering the motional degrees of freedom is because with them we can simulate a realistic analog block. In this sense, the analog gate input and output will be spin states. Each time
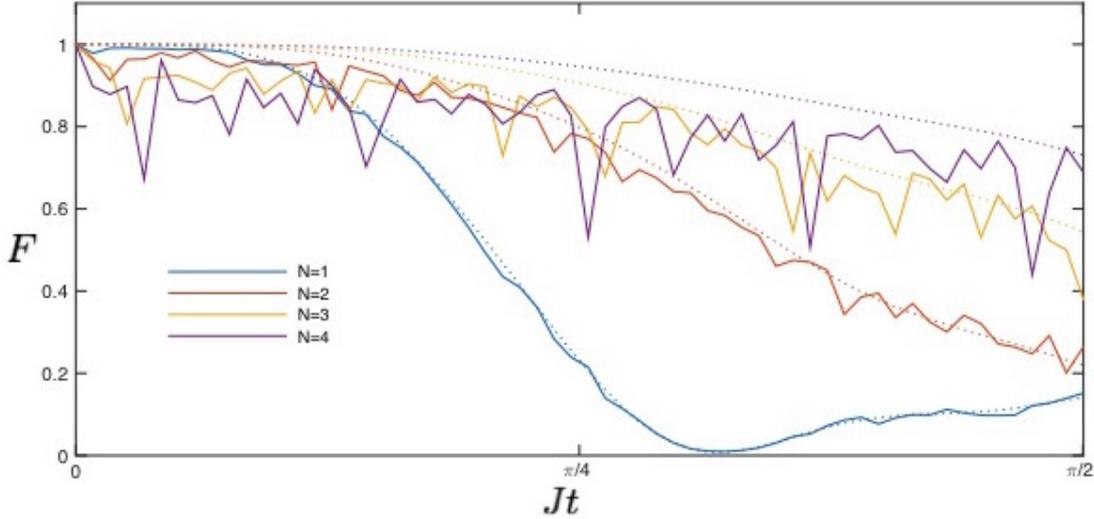
Figure 4.9: Fidelity of initial qubit state $|\downarrow\downarrow\uparrow\downarrow\downarrow\rangle$, with all the motional modes in the ground state, $|0\rangle^{\otimes m}$, evolving under P1 for different Trotter steps N. Solid lines are calculated using trapped-ion Hamiltonian 4.12 as analog block under the following parameter values: $\Omega = (2\pi)125$ kHz, $\Delta = 120$ kHz. Dot lines are the fidelities obtained by considering a perfect analog block.

that an analog gate acts on a spin state we will assume that the radial modes start on the ground state $|0\rangle^{\otimes m}$, and we are not going to care about the final motional state, assuming that these states are barely excited in the process.

In Fig. 4.9, we plotted some numerical results obtained for 5 ions. We show in solid lines the fidelity of a state evolving under our protocol for a different number of Trotter steps. Dotted lines show the fidelity of the state considering only the digital error. Increasing the number of Trotter steps will improve the Trotter error, but will increase the error coming from the imperfect gates. We are thus forced to look for an optimal number of Trotter steps, finding a compromise between these two error sources. The fidelity of single-qubit gates is in general very high, but the analog blocks in our protocol result from an effective second order Hamiltonian, and their fidelity is thus subject to the degree of accuracy of the involved approximations. In our case, these approximations are well fulfilled when the detuning of the lasers with respect to the mode frequencies, Δ, is much larger than the effective second-order coupling, J, which depends on the Rabi frequency, the Lamb-Dicke parameter and Δ itself. This means that the greater Δ the better the gate fidelities, but the longer the simulation time, because J and Δ are inversely related. We are thus limited by the coherence times of the system to make Δ as large as we want. For our simulation we have considered maximum real time simulations of around 50ms. Gate fidelities would improve if longer times were allowed.

From Fig. 4.9 we can see that for short times, a smaller number of Trotter steps results in higher fidelities, while for longer times more Trotter steps are needed. This

suggests that a clever strategy could be to divide the time interval in regions and to simulate each region with the optimal number of Trotter steps, in order to maximize the fidelity during the whole simulation.

In conclusion, our numerical simulation show that with current experimental parameters, times of the order of $10 - 100$ ms are needed to carry out our protocols for 5 ions with final fidelities of around 80%. As the duration of the analog block does not depend on the number of ions, we expect the times to be similar for more ions.

4.5   Experimental considerations

In this section, we will discuss the main experimental limitations that the current trapped-ion technology can show in the task of carrying out our proposal. Let us start from the spin-spin interaction range J_{ij}. Experimentally, the spin-spin coupling strength decays approximately as a power-law function of the distance $|i - j|$

$$J_{ij} \sim J/|i - j|^{\alpha}, \tag{4.20}$$

where α can go in principle form 0 (infinite range) to 3 (short-range) [40] [39]. This α depends mainly on the distance between the ions. If we bring the ions nearer to each other, α will get smaller and, thus, the spin-spin coupling will have a longer range. This distance between the ions depends fundamentally on the axial trapping frequency ω_z. In linear ion traps this frequency is always the lowest one, and in order to maintain the ions in a string, it has an upper bound. While for two ions frequencies of $(2\pi)1.2$MHz can be reached, for 20 ions $(2\pi)0.2$MHz is a maximum value. In this sense, α, and therefore the models that are possible to simulate, are limited by the number of ions.

In Fig. 4.10, we can see how the coupling strength decays in a real ion trap, for the case of 7 ions. For $\omega_z = (2\pi)0.05$ MHz (red line), the shorten range case, we observe that the expression 4.20 is a quite good approximation. For the other cases the approximation is not that good, but we can say that α can reach almost all values from 0.5 to 3. In the case of 20 ions, we can hardly go beyond $(2\pi)0.20$ MHz and this causes the range of α to be smaller. However, still we could tune values approximately from 1 to 2.5. As we may notice, with 20 ions we still can simulate models with a short-range ($\alpha \approx 1$) spin-spin interaction. As a result, we can conclude that these effective spin-spin couplings in trapped ions happen to be are a natural tool to simulate both short-range and long-range spin models.

On the previous section we have performed numerical simulations taking into account protocol P1. However, considering the advantages of using P4, in a real experiment we would recommend to use this last protocol. In protocol P1 H_{xx} and H_{yy} analog blocks are used, which are produced in the same way, except a change in the laser phases. To follow P4 we need to generate H_{xx} and H_{xy} analog blocks, and for the last one, we assume that a centre line detuning of $\delta = (2\pi)3$ kHz is enough to fulfil the condition $\delta \gg J$.
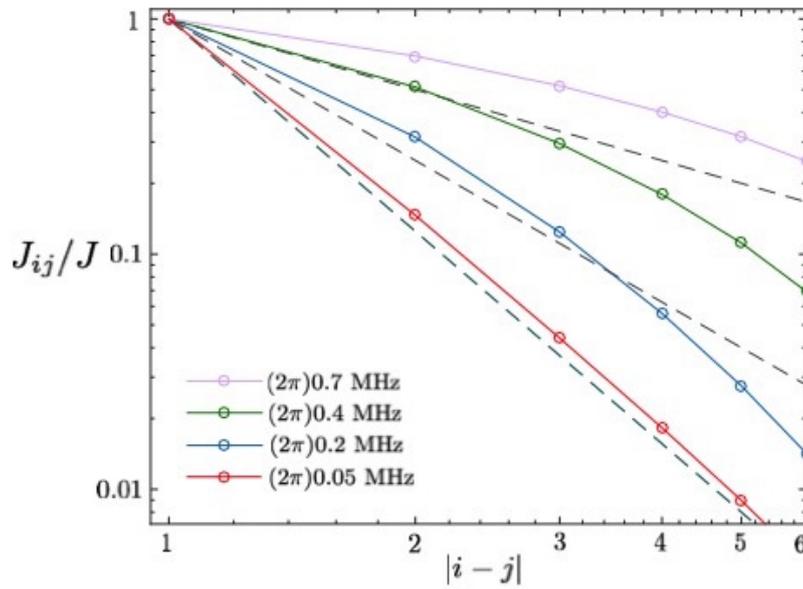
Figure 4.10: Spin-Spin coupling strength J_{ij} for different axial frequencies for 7 ions. Color solid lines correspond to different axial trapping frequencies. Grey dash lines correspond to the coupling strength function characterized by $\alpha = 1, 2, 3$ respectively.
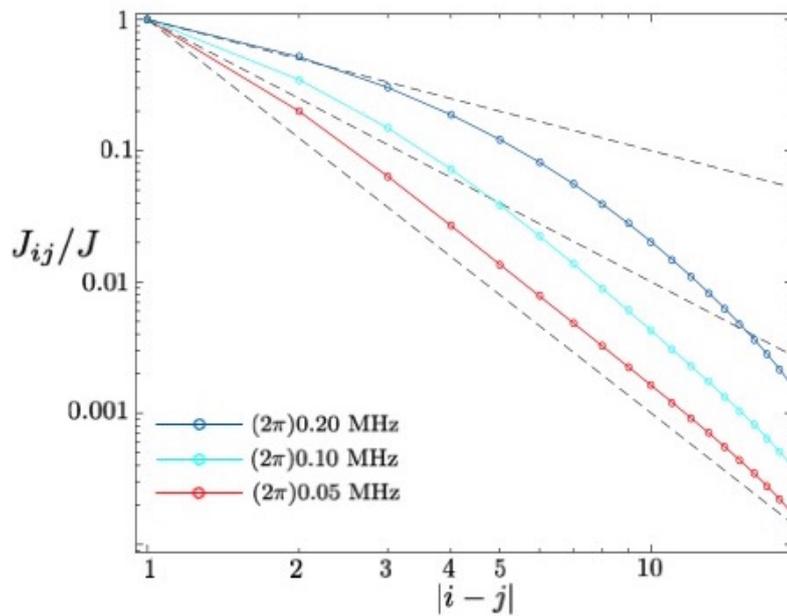

Figure 4.11: Spin-Spin coupling strength J_{ij} for different axial frequencies for 20 ions.

The main limitation of the proposal, however, is related with Δ and the coherence time of the simulation. The coupling strength of our effective interaction is approximately inversely proportional to Δ. On the other hand, the analog gate fidelity gets better when we increase the value of Δ. We want our gate fidelities to be the best possible, but this makes the interaction constant J_{ij} small and thus the simulation very slow. So we are limited by the coherence times of the system to make Δ as large as we want.

As we have seen, $10 - 100$ms are needed to perform our digital-analog quantum simulation. Although we have carried out the simulation for P1, this holds more or less for every protocol. Currently, trapped-ion systems reach $1 - 10$ms of coherence times [46]. They can reach more than 100ms if the dynamics take place in a decoherence-free subspace (DFS) [40]. This happens basically when the Hamiltonian that rules the evolution commutes with $S^z = \hbar/2 \sum_i \sigma_i^z$. For example, the H_{xy} analog block commutes with S^z, so its dynamics will take place in a DFS. The Heisenberg Hamiltonian also has this property, but our digital-analog protocols deals with qubit rotations and Ising-like gates that do not. We would have to engineer an interaction of the type H_{zz} instead of H_{xx}, and in this way the protocol would commute with S^z at every moment. Unfortunately we do not know of any effective interaction of this type in trapped ions, so new ideas are desirable.

Finally, we should also comment that the digital-analog protocols presented in section 4.2 are also valid to simulate anisotropic Heisenberg models. P1 can in principle be used to simulate an anisotropic XYZ Heisenberg spin-1/2 chain. The same with P4, but in this case we are restricted only to the XXZ spin-1/2 chain, which have commented in chapter 2.

Chapter 5

Conclusions

In this thesis, we have proposed a method to study the physics of the spin-1/2 Heisenberg chain in trapped ions. We have explained how to go from long-range spin-spin couplings (LMG) to the shortest range couplings (NN), providing also the possibility of studying, at least approximately, models such as the Majumdar-Ghosh model.

This work introduces a novel simulation method, namely the digital-analog approach. This method takes advantage of the effective many-body spin interactions that can be engineered in trapped ions by tuning the lasers in highly off-resonant red and blue sidebands, and uses them as analog blocks added by digital steps in a global quantum algorithm, to generate the desired Heisenberg evolution. In section 4.2, we first consider different possible decompositions in terms of these analog blocks, and we compare them, taking into account their Trotter error. We conclude that protocol P4 is the most efficient one for the simulation of the Heisenberg model and useful also for simulating more general models such as the anisotropic XXZ chain.

In chapter 4.3, we compare our proposal to other possible purely digital decompositions of the dynamics, i.e., with single and two-qubit gates. Regarding digital error, these fully digital protocols typically involve a higher Trotter error than the digital-analog ones. In Figs. 4.7 and 4.8, we see that the results of the fully digital protocols, with the considered gate fidelities, are only comparable in the case of 4 spins. Once we go beyond $N_s = 4$, the digital-analog protocol maintains similar fidelities, while the fully digital protocol loses quality. This loss of fidelity is more dramatic when we enlarge the interaction range. As a result, we conclude that the proposed digital-analog simulation enjoys improved scalability features than a fully digital simulation, taking into account realistic gate fidelities.

In chapter 4.4, we have carried out a numerical simulation of our digital-analog proposal using a first-principles trapped-ion Hamiltonian. We have developed a method that allows us to simulate the action of an analog block of more than 7 spins, considering all vibrational and internal degrees of freedoms of the ions. Using this method we have been able to conclude that with current experimental parameters, times of the order of $10 - 100$ ms are needed to carry out our protocols with final fidelities of around 80%. These coherence times are in the limit of actual experimental capabilities, which are

expected to improve in the near future.

Finally, we have investigated also how the increasing number of ions/spins N_s may affect the variety of the models that we can have access to, characterized by $J_{ij} \sim J/|i-j|^{\alpha}$ and bounded by the possible values of α. We have concluded that, although the simulation of the LMG model ($\alpha = 0$) for 20 ions seems unfeasible, we can study various interesting Heisenberg spin models, which go from short-range cases ($\alpha \approx 2.5$) to long-range ones ($\alpha \approx 1$), each of them with similar efficiency. This does not hold for fully digital cases, where to enlarge the interaction range, means to introduce more gates and therefore to increase the error.

All in all, the presented digital-analog apprach shows to be a suitable alternative to purely digital protocols, which suffer from higher experimental errors due to the greater number of gates involved, as well as a higher error coming from the digitization of the dynamics. In the same way, existing analog proposals also face difficulties in the experimental arena due to decoherence rates of the involved degrees of freedom, which may be overcome with our proposal.

Focusing on the importance of profiting from the complexity of the dynamics already present in the simulator, digital-analog techniques offer a good compromise between the capabilities of simulation and the experimental requirements of the simulator. In this sense, we believe that digital-analog techniques will prove to be a relevant approach to quantum simulation in the near future. As these concepts are platform independent, this work paves the way for the application of these ideas in the simulation of different models and in different platforms.

Acknowledgments

First, I would like to thank Prof. Enrique Solano for giving me the opportunity to join the QUTIS group, and also for sharing with the youngest his special view about physics and its people.

I would also want to thank Dr. Lucas Lamata, whose "trapped-ion smile" shows that it is worth working in this field.

I specially thank Julen S. Pedernales for his daily enthusiasm, infinite patience and for turning anything a little bit simpler.

Last but not least, I thank all QUTISers, that create such a friendly working environment, and in general every saint and sinner that has ever enjoyed talking physics with me.

Bibliography

[1] R. Feynman, Int. J. Theor. Phys. **21**, 467 (1982).

[2] P. W. Shor, SIAM J. Comput. **26**(5), 1484 (1997).

[3] C. H. Bennett, G. Brassard, Proceedings of IEEE International Conference on Computers, Systems and Signal Processing **175**, 8 (1984).

[4] C. H. Bennett, G. Brassard, C. Crépeau, R. Jozsa, A. Peres, and W. K. Wootters, Phys. Rev. Lett. **70**, 1895 (1993).

[5] J. I. Cirac and P. Zoller, Phys. Rev. Lett. **74**, 4091 (1995).

[6] H. Häffner, C. R. Ross, and R. Blatt, Phys. Rep. **469**, 155 (2008).

[7] J. Casanova, A. Mezzacapo, L. Lamata, and E. Solano, Phys. Rev. Lett. **108**, 190502 (2012).

[8] L. Lamata, J. León, T. Schätz, and E. Solano, Phys. Rev. Lett. **98**, 253005 (2007).

[9] M. Pons, V. Ahufinger, C. Wunderlich, A. Sanpera, S. Braungardt, A. Sen(De), U. Sen, M. Lewenstein, and Phys. Rev. Lett. 98, 023003 (2007).

[10] D. Leibfried, R. Blatt, C. Monroe, and D. J. Wineland, Rev. Mod. Phys. **75**, 281 (2003).

[11] T. P. Harty, D. T. C. Allcock, C. J. Ballance, L. Guidoni, H. A. Janacek, N. M. Linke, D. N. Stacey, and D. M. Lucas, Phys. Rev. Lett. **113**, 220501 (2014).

[12] C. J. Ballance, T. P. Harty, N. M. Linke, and D. M. Lucas, arXiv:1406.5473 (2014).

[13] D. Porras and J. I. Cirac, Phys. Rev. Lett. **92**, 207901 (2004).

[14] J. J. García-Ripoll, M. A. Martin-Delgado, and J. I. Cirac, Phys. Rev. Lett. **93**, 250405 (2004).

[15] A. Friedenauer, H. Schmitz, J. T. Glückert, D. Porras, and T. Schätz, Nat. Phys. **4**, 757 (2008).

[16] K. Kim, M.-S. Chang, S. Korenblit, R. Islam, E. E. Edwards, J. K. Freericks, G.-D. Lin, L.-M. Duan, and C. Monroe, Nature (London) **465**, 590 (2010).

[17] B. P. Lanyon, C. Hempel, D. Nigg, M. Müller, R. Gerritsma, F. Zähringer, P. Schindler, J. T. Barreiro, M. Rambach, G. Kirchmair, M. Hennrich, P. Zoller, R. Blatt, and C. F. Roos, Science **334**, 57 (2011).

[18] Y. Salathé, M. Mondal, M. Oppliger, J. Heinsoo, P. Kurpiers, A. Potŏcnik, A. Mezzacapo, U. Las Heras, L. Lamata, E. Solano, S. Filipp, and A. Wallraff, Phys. Rev. X **5**, 021027 (2015).

[19] S. Lloyd, Science **273**, 1073 (1996).

[20] J. I. Cirac and P. Zoller, Nature Phys. **8**, 264 (2012).

[21] I. M. Georgescu, S. Ashhab, and F. Nori, Rev. Mod. Phys. 86, 153 (2014).

[22] D. P. DiVincenzo, arXiv:1304.2322 (2000).

[23] M. Nielsen, I. Chuang, *Quantum Computation and Quantum Information* (Cambridge University Press, Cambridge, 2000).

[24] H. F. Trotter, Proc. Am. Math. Soc. **10**, 545 (1959).

[25] R. Gerritsma, G. Kirchmair, F. Zähringer, E. Solano, R. Blatt, and C. F. Roos, Nature (London) **463**, 68 (2010).

[26] R. Gerritsma, B.P. Lanyon, G. Kirchmair, F. Zähringer, C. Hempel, J. Casanova, J.J. García-Ripoll, E. Solano, R. Blatt, and C.F. Ross, Phys. Rev. Lett. **106**, 060503 (2011).

[27] D. C. Mattis, *The Theory Of Magnetism Made Simple* (World Scientific, USA).

[28] G. E. Uhlenbeck and S. Goudsmit, Nature (London) **117**, 264 (1926).

[29] P. A. M. Dirac, Proc. Roy. Soc. **117A** 610 (1928).

[30] H. Bethe, Z. Phys. **71**, 205 (1931).

[31] M. Karbach, G. Müller, arXiv:cond-mat/9809162 (1998).

[32] C. K. Majumdar and D. K. Ghosh, J. Math. Phys. **10**, 1388 (1969).

[33] A. Auerbach, *Interacting Electrons and Quantum Magnetism* (Springer-Verlag, Berlin, 1994).

[34] K. Okamoto and K. Nomura, Phys. Lett. A **169**(6), 433 (1992).

[35] K. Nomura and K. Okamoto, J. Phys. A: Math. Gen. **27**, 5773 (1994).

[36] H. Lipkin, N. Meshkov, and A. J. Glick, Nucl. Phys. **62**, 188 (1965).

[37] M.-H. Yung, J. Casanova, A. Mezzacapo, J. McClean, L. Lamata, A. Aspuru-Guzik, and E. Solano, Sci. Rep. **4**, 3589 (2014).

[38] K. Kim, M.-S. Chang, R. Islam, S. Korenblit, L.-M. Duan, and C. Monroe, Phys. Rev. Lett. **103**, 120502 (2009).

[39] P. Richerme, Z.-X. Gong, A. Lee, C. Senko, J. Smith, M. Foss-Feig, S. Michalakis, A. V. Gorshkov, and C. Monroe, Nature (London) **511**, 198 (2014).

[40] P. Jurcevic, B. P. Lanyon, P. Hauke, C. Hempel, P. Zoller, R. Blatt, and C. F. Roos, Nature (London) **511**, 202 (2014).

[41] P. Jurcevic, P. Hauke, C. Maier, C. Hempel, B. P. Lanyon, R. Blatt, and C. F. Roos, Phys. Rev. Lett. **115**, 100501 (2015).

[42] A. Steane, Appl. Phys. B **64**, 623 (1997).

[43] D. F. V. James, Appl. Phys. B: Lasers Opt. **B66**, 181 (1998).

[44] T. Graß and M Lewenstein, EPJ Quantum Technology **1**, 8 (2014).

[45] I. Cohen, P. Richerme, Z.-X. Gong, C. Monroe, and A. Retzker, Phys. Rev. A **92**, 012334 (2015).

[46] R. Islam, C. Senko, W. C. Campbell, S. Korenblit, J. Smith, A. Lee, E. E. Edwards, C.-C. J. Wang, J. K. Freericks, and C. Monroe, Science **340**, 583 (2013).